

RESEARCH ARTICLE

10.1002/2013JB010773

Key Points:

- Variable resolution model of global radial shear wave anisotropy
- Peak in $\xi > 1$ under oceans in better agreement with LAB depths
- $\xi < 1$ near the large low-shear velocity provinces at the CMB

Correspondence to:

L. Auer,
ludwig.auer@tomo.ig.erdw.ethz.ch

Citation:

Auer, L., L. Boschi, T. W. Becker, T. Nissen-Meyer, and D. Giardini (2014), *Savani*: A variable resolution whole-mantle model of anisotropic shear velocity variations based on multiple data sets, *J. Geophys. Res. Solid Earth*, 119, 3006–3034, doi:10.1002/2013JB010773.

Received 13 OCT 2013

Accepted 16 FEB 2014

Accepted article online 27 FEB 2014

Published online 2 APR 2014

Savani: A variable resolution whole-mantle model of anisotropic shear velocity variations based on multiple data sets

L. Auer¹, L. Boschi^{2,3}, T. W. Becker⁴, T. Nissen-Meyer⁵, and D. Giardini¹

¹Institut für Geophysik, Eidgenössisch Technische Hochschule, Zürich, Switzerland, ²Sorbonne Universités, UPMC Univ Paris 06, Institut des Sciences de la Terre Paris (iSTeP), Paris, France, ³CNRS, Institut des Sciences de la Terre Paris (iSTeP), Paris, France, ⁴Department of Earth Sciences, University of Southern California, Los Angeles, California, USA, ⁵Department of Earth Sciences, University of Oxford, Oxford, UK

Abstract We present a tomographic model of radially anisotropic shear velocity variations in the Earth's mantle based on a new compilation of previously published data sets and a variable block parameterization, adapted to local raypath density. We employ ray-theoretical sensitivity functions to relate surface wave and body wave data with radially anisotropic velocity perturbations. Our database includes surface wave phase delays from fundamental modes up to the sixth overtone, measured at periods between 25 and 350 s, as well as cross-correlation traveltimes of major body wave phases. Before inversion, we apply crustal corrections using the crustal model CRUST2.0, and we account for azimuthal anisotropy in the upper mantle using ray-theoretical corrections based on a global model of azimuthal anisotropy. While being well correlated with earlier models at long spatial wavelength, our preferred solution, *savani*, additionally delineates a number of previously unidentified structures due to its improved resolution in areas of dense coverage. This is because the density of the inverse grid ranges between 1.25° in well-sampled and 5° in poorly sampled regions, allowing us to resolve regional structure better than it is typically the case in global S wave tomography. Our model highlights (i) a distinct ocean-continent anisotropic signature in the uppermost mantle, (ii) an oceanic peak in above average $\xi < 1$ which is shallower than in previous models and thus in better agreement with estimates of lithosphere thickness, and (iii) a long-wavelength pattern of $\xi < 1$ associated with the large low-shear velocity provinces in the lowermost mantle.

1. Introduction

In the last decades, independently derived tomography models of isotropic whole-mantle shear wave velocity variations have advanced to a state of considerable consistency, in terms of the geographic pattern, and, to some extent, the amplitude of velocity heterogeneity. The long-wavelength robustness of global tomographic models has allowed for a number of subsequent studies, aimed at reconciling seismological results with dynamic models of mantle convection [e.g., *Mégnin et al.*, 1997; *Becker and Boschi*, 2002; *Ritsema et al.*, 2007; *Boschi et al.*, 2008; *Bull et al.*, 2010]. However, the majority of seismic models used in such comparative studies are based on the assumption of isotropic wave propagation, or no lateral variation in anisotropy, and no mantle anisotropy other than the global average, uppermost mantle radial anisotropy included in the preliminary reference Earth model (PREM) [*Dziewoński and Anderson*, 1981]. This description is known to be inadequate at various locations in the mantle [*Anderson and Dziewoński*, 1982]. The elastic anisotropy of Earth's materials manifests itself in a number of seismological observations: The azimuthal discrepancies of *P_n* traveltimes [e.g., *Hess*, 1964; *Raitt et al.*, 1971], the variation of Rayleigh wave phase velocities with azimuth (direction of propagation) [*Forsyth*, 1975], and the splitting of shear wave phases in fast and slow polarization directions [*Vinnik et al.*, 1984; *Silver*, 1996]. Most mantle-based anisotropy is related to mantle flow via the alignment of intrinsically anisotropic minerals, and anisotropy is thus a useful proxy for mantle convection [e.g., *Long and Becker*, 2010].

Recently, there have been some steps forward in imaging radial anisotropy at a whole-mantle scale [*Boschi and Dziewoński*, 2000; *Gung et al.*, 2003; *Soldati et al.*, 2003; *Panning and Romanowicz*, 2006; *Kustowski et al.*, 2008], and several authors have attempted to relate those tomographic results with models of mantle flow and texture generation in the upper mantle [e.g., *Becker et al.*, 2008; *Schaefer et al.*, 2011] and the D'' region

[Walker et al., 2011], which lead to progress in understanding a number of observations, such as the $\xi < 1$ anomaly at the center of the Pacific Ocean [Ekström and Dziewonski, 1998].

Here we present a new method to map whole-mantle isotropic variations of the average (Voigt) shear wave speed and radial anisotropy as parameterized by $\xi = (v_{SH}/v_{SV})^2$ using a multiscale tomographic inversion approach of laterally variable resolution. We then seek to address the following questions: How coherent is anisotropy as mapped by various surface wave data sets? Is it possible to combine such data sets to enhance resolution? How important is it to account for inhomogeneities in global data coverage, particularly when mapping anisotropic structure? How strong are the trade-offs between isotropic and anisotropic structure or azimuthal and radial anisotropy?

Our main result is the anisotropic whole-mantle model *savani* (S wave, adaptive, voxel, anisotropic), based on a data-adaptive variable block parameterization. We use multiple data sets, some of which have not been explored for anisotropy before, and we correct them for azimuthal anisotropy in the uppermost mantle which is crucial to reduce artifacts [Ekström, 2011]. We present a comprehensive comparison between recent upper and whole-mantle radially anisotropic (and isotropic) models to identify a number of regions in the mantle in which anisotropic tomography has advanced to a state of maturity, comparable to that of its isotropic counterpart.

2. Methodology

Smith and Dahlen [1973] showed that surface wave propagation in weakly anisotropic media having a hexagonal axis of symmetry is governed by a subset of 13 of the full 21 elements of the elastic tensor. To reduce the number of unknowns in the inversion, usually either a horizontal (azimuthal anisotropy) or a vertical axis of symmetry (transverse isotropy or radial anisotropy) is assumed. Pure azimuthal anisotropy is usually considered when only inverting vertically polarized (Rayleigh) waves. In this case, only three elastic parameters remain [e.g., Montagner and Nataf, 1986].

In joint inversions of vertically (Rayleigh) and horizontally polarized (Love) waves, it turns out that the radially anisotropic parameters are most important to find a model which explains both types of data at the same time. Therefore, it is often assumed that azimuthal anisotropy is small or averaged out sufficiently by a good azimuthal coverage [Montagner and Anderson, 1989]. In transversely isotropic media the elasticity tensor reduces to the five parameters A, C, N, L, and F [Love, 1927], which relate to velocities as $\rho v_{PH}^2 = A$, $\rho v_{PV}^2 = C$, $\rho v_{SH}^2 = N$, $\rho v_{SV}^2 = L$, with closed measures of anisotropy $\xi = v_{SH}^2/v_{SV}^2 = N/L$, $\phi = v_{PH}^2/v_{PV}^2 = A/C$, $\eta = F/(A - 2L)$.

To be able to directly damp upon anisotropic structure, we reparameterize our sensitivity kernels in average isotropic and anisotropic parameters following Ferreira et al. [2010] as $v_S^2 = 0.5(v_{SH}^2 + v_{SV}^2)$ and $\Xi_S = (v_{SH}^2 - v_{SV}^2)/2v_S$. A number of authors have shown that inverting separately for the differently polarized components v_{SH} and v_{SV} , and deriving anisotropic and isotropic variations by composing the two in a secondary step can lead to presumably unrealistically high roughness in the anisotropic component [e.g., Nettles and Dziewoński, 2008]. Nevertheless, we also perform separate inversions in v_{SH} and v_{SV} to check the general consistency of the results. Before plotting and analyzing our results, we reparameterize in terms of Voigt average $v_S = \sqrt{\frac{2v_{SV}^2 + v_{SH}^2}{3}}$ and ξ , since such averaging is known to better reflect the overall macroscopic isotropic elastic properties [Babuška and Cara, 1991].

2.1. Surface Wave Theory

Our modeling procedure is based on that of, e.g., Boschi and Ekström [2002] and Boschi et al. [2009]. We include surface wave fundamental-mode and overtone information in the form of path-averaged phase delays and employ Fermat's principle to linearly relate the phase anomaly $\delta\Phi_j$ of a certain surface wave mode to three-dimensional distribution of i th parameter heterogeneity $\delta p_i(r, \theta, \phi)$ via the sensitivity kernel K_i

$$\frac{\delta\Phi_j(\omega)}{\omega} = \sum_{i=1}^I \sum_{k=1}^K x_{ik} \int_0^{\Delta_j} \int_0^a K_i(r; \omega) f_k(r, \theta, \phi) dr ds \quad (1)$$

where r denotes radius, Δ_j is the epicentral distance associated with raypath j , a is the radius of the Earth's outer surface, θ longitude, ϕ latitude, and ω the angular frequency. $j = 1, \dots, M$ represents an additional

subscript over the M measurements. In equation (1) the heterogeneity has been expanded in basis functions $\delta p_i(r, \theta, \phi) \approx \sum_{k=1}^K x_{ik} f_k(r, \theta, \phi)$, where $i = 1, \dots, I$ is the index over the physical parameters and $k = 1, \dots, N$ is the index over the chosen basis function. In our radially anisotropic parameterization, K_j corresponds to sensitivities with respect to the Love coefficients, density ρ , and two attenuation parameters [e.g., *Montagner and Nataf*, 1986]. It is straightforward to recast expression (1) in terms of more physically meaningful parameters such as horizontally and vertically polarized wave speed v_{SH} , v_{SV} and v_{PV} , v_{PH} , respectively.

Surface waves have little sensitivity to P wave speed v_p and density ρ , and instead of jointly inverting for these parameters together with v_s , it is common practice to neglect v_p and ρ sensitivity or to impose a laboratory-based mineralogical scaling law that constrains them to v_s . While such scaling laws may be petrologically meaningful in the upper mantle [*Montagner and Anderson*, 1989; *Becker et al.*, 2006], little is known about equivalent correlations for the lower mantle, and choosing a single scaling factor in the entire mantle is probably inadequate [*Simmons et al.*, 2010]. *Boschi and Ekström* [2002] have verified that scaling P wave sensitivity to S wave sensitivity using constant factors between ~ 0.5 and 1.0 [*Anderson and Isaak*, 1995] does not substantially alter the results of fundamental-mode surface wave tomography. Here we have chosen an even simpler approach: we neglect v_p sensitivity completely. This could lead to some artifacts, e.g., under areas like cratons, where very high v_p partly accounts for high Rayleigh-wave phase velocities; this effect is however presumably limited to shallow depths and comparable to (possibly smaller) errors due to the limited quality of reference crustal models. In future work, we shall improve shallow structure regionally, making use of higher-resolution crustal models, surface wave data extracted from ambient noise, and a more careful account of v_p sensitivity.

In Figure 1 we show sensitivity kernels at a location near Antarctica (where the crust is around ~ 25 km deep) for a dominant period of 100 s. Surface wave sensitivities have a complex frequency and depth dependency [*Dahlen and Tromp*, 1998]. To first order, the highest peak in sensitivity of fundamental-mode surface waves, which we compute numerically in the framework of a Jeffreys-Wentzel-Kramers-Brillouin (JWKB) description of surface wave propagation [e.g., *Boschi and Ekström*, 2002], is found at larger depth and is weaker, with decreasing frequency. Rayleigh waves have little sensitivity to v_{SH} , while Love waves have less sensitivity to v_{SV} . In the frequency range at which data are available to us, fundamental-mode sensitivity (Figure 1, black lines) is significant down to a depth of ~ 250 km. Overtones (Figure 1, gray lines) show a more variable and complex pattern of sensitivity but have significant sensitivity down to a depth of ~ 1000 km.

2.2. Body Wave Theory

In a relatively smooth medium for which ray theory is an adequate description of wave propagation, the j th traveltime perturbation δT_j is related to three-dimensional variation of the i th Earth parameters $\delta p_i(r, \theta, \phi)$ through the linearized expression

$$\delta T_j = - \sum_{i=1}^I \sum_{k=1}^K x_{ik} \int_0^{\text{path}_j} G(r; \omega) f_k(r, \theta, \phi) ds \quad (2)$$

similar to (1), with $j = 1, \dots, M$ denoting the observations and $i = 1, \dots, I$ the index over the selected inversion parameters. The integral is now along an infinitesimal thin raypath associated with a certain phase. Again, the parameters $\delta p_i(r, \theta, \phi)$ have been expanded in basis functions $\delta p_i(r, \theta, \phi) \approx \sum_{k=1}^K x_{ik} f_k(r, \theta, \phi)$ with $k = 1, \dots, N$, to make x_{ik} independent of r, θ , and ϕ . The tracing of rays through spherically symmetric transverse isotropic Earth and the associated sensitivity for body wave phases is given in *Woodhouse* [1981], who provide an elegant derivation based on the mode-ray analogy. Toward the ray turning point, v_{SH} sensitivity of direct and multiply-bouncing S phases increases, while v_{SV} sensitivity goes to zero (see Figure 1b). Core-transversing phases SKS and SKKS are the only phases in our database having significant sensitivity to v_{SV} in the lowermost mantle but are insensitive to v_{SH} . We linearize around the radially anisotropic reference model PREM [*Dziewoński and Anderson*, 1981], which includes $\xi > 1$ in the upper 200 km of the mantle.

Like in equation (1), the integral along the path can be translated into matrix form, and thus easily combined with the surface wave terms into the global linear system $\mathbf{A} \cdot \mathbf{x} = \mathbf{d}$, where \mathbf{A} contains partial derivatives and damping constraints, and \mathbf{x} and \mathbf{d} correspond to the model and data vectors, respectively.

2.3. Parameterization

Resolution in global tomography is spatially varying and governed by several of factors, including dominant wavelength, imposed regularization, and—most importantly—the geographical distribution of sources and

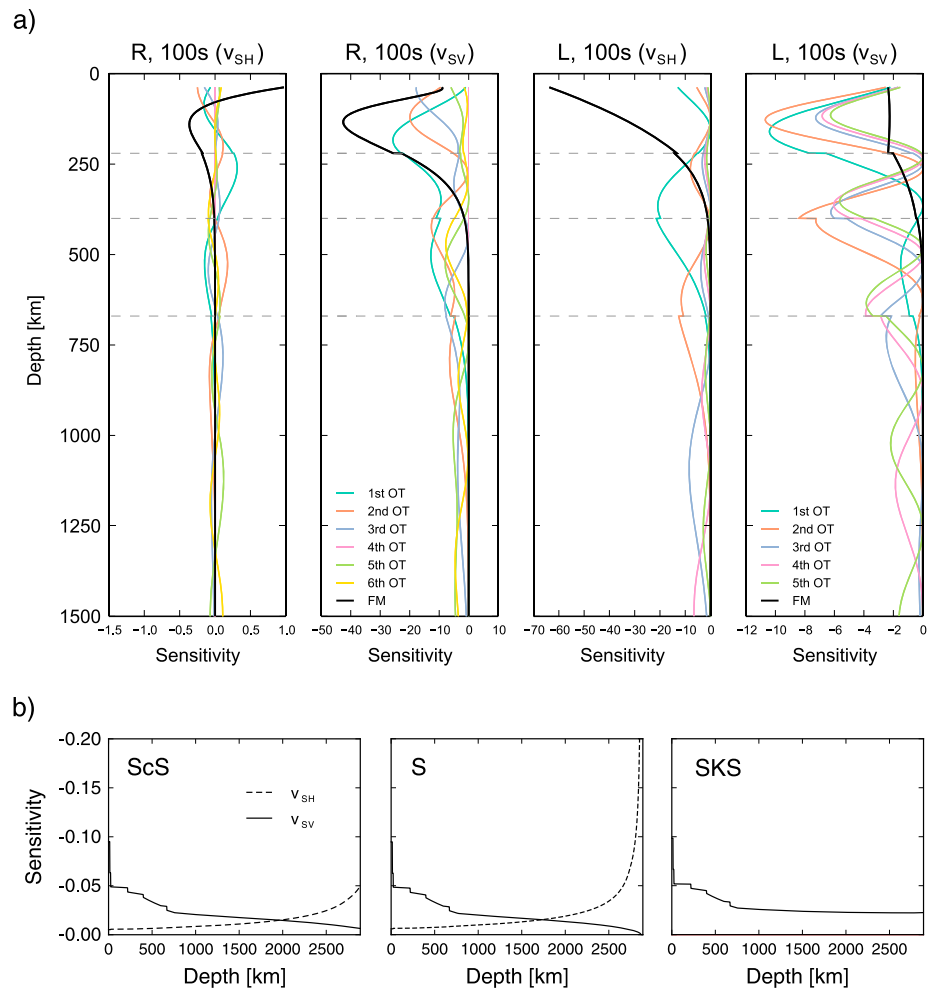


Figure 1. (a) Depth dependence of sensitivity kernels, relating path-averaged phase delays of Love (L) and Rayleigh (R) waves with three-dimensional shear velocity structure (in terms of horizontally and vertically polarized wave speed v_{SH} and v_{SV}). We plot an example at the Antarctic region. Fundamental-mode sensitivities are given in black lines, and overtone sensitivities are drawn in color. Note the different scales in the first through the fourth panels. (b) Body wave sensitivity of selected shear wave phases. Sensitivity to v_{SH} is given by the dashed lines, and sensitivity to v_{SV} is given by solid lines. SKS is the only phase with significant sensitivity to v_{SV} in the core-mantle boundary region.

receivers. One can choose amongst a wide variety of basis function to adequately describe a model: lateral and vertical splines [e.g., Panning *et al.*, 2010; Kustowski *et al.*, 2008; Nettles and Dziewoński, 2008; French *et al.*, 2013; Boschi *et al.*, 2004], spherical harmonics [e.g., Ritsema *et al.*, 2011; Ferreira *et al.*, 2010], triangles and layers [e.g., Schaeffer and Lebedev, 2013], tetrahedra [e.g., Sigloch, 2011], wavelets [Simons *et al.*, 2011], or “blocks” [e.g., Boschi and Becker, 2011; Simmons *et al.*, 2010].

Irregular data coverage is often neglected in the model space design, but a number of authors address the issue by multiresolution parameterization schemes, spatially varying regularization weights, or down-weighting of repeating raypaths [Lekić and Romanowicz, 2011]. Some multiresolution studies employ manual local grid refinement [e.g., Boschi *et al.*, 2004; Nettles and Dziewoński, 2008], while others use data-adaptive schemes [e.g., Bijwaard *et al.*, 1998; Li *et al.*, 2008; Schaefer *et al.*, 2011]. We follow the approach of Schaefer *et al.* [2011] and use variable size blocks (pixels) and layers to expand our basis functions. Pixel size is adapted to sampling density, and we extended the work of Schaefer *et al.* [2011] by allowing for vertical variations in mesh density, which is important when the joint inversion of surface and body waves is considered. We first compute sensitivities on a $1.25^\circ \times 1.25^\circ$ grid and subsequently merge horizontally adjacent blocks up to a final size of $5^\circ \times 5^\circ$, as long as their coverage (defined by the number of rays hitting each block and

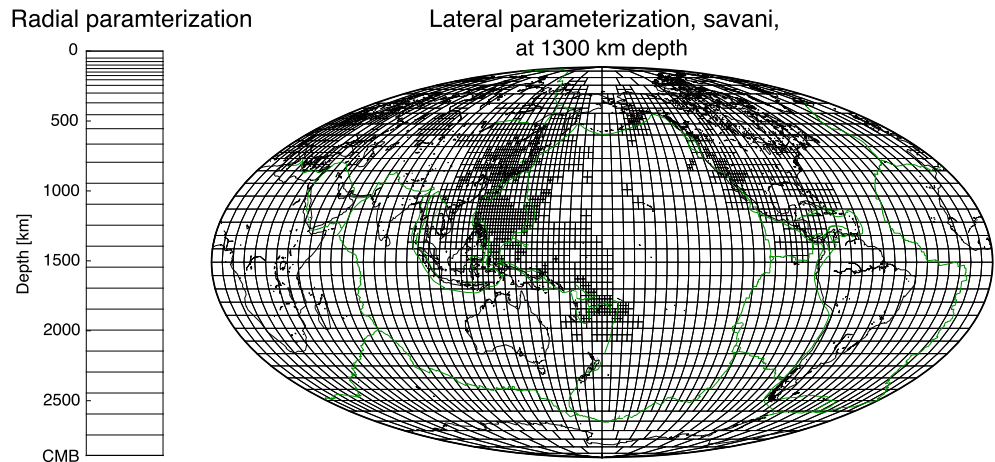


Figure 2. Radial and lateral parameterization corresponding to model C (*savani*) at a depth of 1300 km. Due to increased sampling density, a number of regions are refined with respect to $5^\circ \times 5^\circ$ down to a lateral grid spacing of $1.25^\circ \times 1.25^\circ$. Thickness of the 28 vertical layer thickness is chosen apriorily and refined in the upper mantle. In total, model C is based on $\sim 200,000$ free parameters.

the azimuthal uniformity of ray coverage) exceeds a certain threshold value. While body wave hitcounts can be used directly in this procedure, surface wave hitcounts are multiplied by a depth-dependent factor, so as to account for the decrease of K_i with depth (see section 2.1).

Our $5^\circ \times 5^\circ$ base grid is approximately equivalent to a degree 40 spherical harmonic parameterization, with a nominal resolution comparable to that of most recent whole-mantle shear velocity models. In Figure 2 we exemplify our parameterization approach on a multiscale grid, originating from a combination of the data sets of Ekström [2011], Visser et al. [2008a], and Ritsema et al. [2011]. Adaptive parameterization as applied here can be seen as an efficient way of regularizing our inverse problem: in fact, variable resolution could also be achieved by spatially varying regularization constraints. Yet, since our approach involves the least squares solution of the rectangular tomographic system $A^{-1}d = m$, simply varying the smoothing weights would yield unnecessarily large matrices in the case of a whole-mantle $1.25^\circ \times 1.25^\circ$ parameterization.

2.4. The Inverse Problem

We combine the total linear system resulting from equations (1) and (2) in the matrix expression

$$\begin{pmatrix} w_1 A_{SW} \\ w_2 A_{BW} \\ \mu G \end{pmatrix} \cdot x = \begin{pmatrix} w_1 d_{SW} \\ w_2 d_{BW} \\ 0 \end{pmatrix} \quad (3)$$

with x the model vector, and SW and BW denote the body wave and the surface wave fractions of our data set, respectively. The w_1 and w_2 denote factors, which allow to give certain fractions of the database larger or smaller weights. The operator G gives a measure of the roughness of the model vector to which it is applied. Following Boschi and Dziewoński [2000], we define G by minimizing the finite difference in m between neighboring voxels [e.g., Menke, 1989]. By least squares-solving equation (3) we constrain m to fit the data and, through the cost function $|Gx|$, to be locally smooth [Nolet, 2008].

Adjusting the value of μ , we can explore possible solution models of variable roughness. We solve our sparse system in a least squares sense using LSQR [Paige and Saunders, 1982]. Solving equation (3) is computationally expensive: In case of our largest runs (i.e., involving the full database of $\sim 10^7$ measurements) one inversion takes around 24 h on a single CPU and consumes up to ~ 200 GB of RAM. As a measure of data fit and model quality we use the variance reduction VR which is defined as,

$$VR = 1 - \frac{\sum_{i=1}^m ((A \cdot x)_i - d_i)^2}{\sum_{i=1}^m d_i^2} \quad (4)$$

Table 1. Overview of Surface Wave Data Sets Employed in This Study^a

Author	SPH	SR	TOR	SR
<i>Ritsema et al.</i> [2004]	FM 37–374 s	2,977,971	FM 37–375 s	1,605,517
	First OT 37–274 s	391,495	First OT 37–269 s	666,057
	Second OT 37–365 s	343,398	Second OT 37–151 s	242,996
	Third OT 37–273 s	316,161	Third OT 37–100 s	118,018
	Fourth OT 37–149 s	300,515	Fourth OT 37–69 s	54,279
	Fifth OT 37–114 s	240,256	Fifth OT 37–56 s	31,106
<i>Visser et al.</i> [2008a]	Sixth OT 37–78 s	162,507		
	FM 35–175 s	477,776	FM 35–173 s	399,792
	First OT 35–149 s	396,431	First OT 35–176 s	331,168
	Second OT 35–149 s	364,140	Second OT 35–115 s	250,315
	Third OT 35–149 s	253,143	Third OT 35–78 s	154,160
	Fourth OT 35–87 s	159,448	Fourth OT 35–62 s	81,592
<i>Ekström</i> [2011]	Fifth OT 35–56 s	114,037	Fifth OT 35–56 s	42,756
	Sixth OT 37–50 s	71,652		
	FM 25 s to 250 s	1,022,706	FM 25 s to 250 s	342,261

^aWe bin all measurements in a summary data set, resulting in a total of ~10,000,000 summary rays (SR). The column under SPH contains spheroidal (Rayleigh wave) measurements, while the column under TOR contains toroidal (Love wave) measurements. The abbreviation FM stands for fundamental modes, while OT denotes overtones.

We plot this measure of data fit against an estimate of model roughness to perform the classical trade-off curve (L curve) analysis to find optimal damping parameters. We define model roughness as the dot product of our gradient damping operator with the resulting model vector m and normalize it by the total RMS average of the model vector.

2.4.1. Regularization

Even though a data-adaptive parameterization represents, by itself, a form of regularization, the sparse linear system (equation (3)) is ill conditioned enough for additional damping/smoothing to be necessary [Bijwaard *et al.*, 1998]. We chose to impose the same horizontal roughness damping constraints on v_{SH} and v_{SV} or, depending on the chosen inversion approach, v_S and Ξ_S . While horizontal roughness damping is constant at all depths, we adapt the vertical smoothing weights so as to account for the smaller vertical resolution at larger depths [Bijwaard *et al.*, 1998]. At shallow depths between 0 and 300 km vertical roughness terms are given a weight of twice (2x) the weight given to horizontal damping terms. At depths larger than 300 km this multiplication factor linearly increases from 2 to a value of 5.

Using a variable grid parameterization entails a number of complications in defining our roughness damping terms. Unlike Schaefer *et al.* [2011], who chose to define smoothing operators for each adaptive pixel in the spherical harmonic domain and subsequently translated them to the pixel basis, we chose to simply identify, for each block, all its direct neighbors and minimize the difference using the expression

$$f \cdot h \cdot \left(x_k - \frac{1}{N} \sum_{l=1}^N x_l \right) = 0 \quad (5)$$

where the value of the weight f depends on whether the lateral or above/below neighbors are considered ($f_{\text{horizontal}} = 1$; $f_{\text{vertical}} = 2, \dots, 5$), and the factor h , which ranges between 0.8 (for the smallest blocks) and 1.0 (for the largest blocks), is proportional to the volume of block k [Bijwaard *et al.*, 1998].

2.4.2. Weighting

We construct our weighting scheme such to achieve a more or less uniform sensitivity with depth [Kustowski *et al.*, 2008] but also account for larger uncertainty associated with certain data types. Generally, we upweigh portions of our data set when the involved number of measurements is smaller and when the delay times of the subgroup are associated with a lower RMS value. We upweigh all body wave data so as to account for the lower absolute number of body wave measurements. As illustrated in Figure 1b, core-transversing phases SKS and SKKS are the only phases in our database having significant sensitivity to v_{SV} in the lowermost mantle. Following Kustowski *et al.* [2008] we give those data a relatively high weight in our inversion. Lastly, we chose to downweigh multiply-bouncing body wave phases [e.g., Simmons *et al.*, 2010] due to their larger

Table 2. Overview of the Body Wave Data Sets Employed in This Study^a

Author	Phase	No.
Ritsema et al. [2011]	S, (Sdiff)	194,488
	SS	125,068
	SSS	28,288
	SKS	35,267
	SKKS	9,183
	ScS, sScS	10,329
	ScS2, ScS3, ScS4 (SSm), (SSSm), (SSSSm)	28,200 28,620
Gu et al. [2005]	S	32,173
	SS	16,137
	ScS	5,521

^aData sets in brackets correspond to diffracted (diff) and major arc (m) phases. We chose not to include major arc data due to the relative high uncertainties associated with such measurements.

errors and downweigh body wave outliers having traveltimes that exceed a phase-specific cutoff value, by multiplying this particular measurement (and the associated sensitivity terms) with the exponential of its excess time. We have conducted extensive testing to identify the range of weighting parameters in which our final solutions do not vary strongly. However, the exact choice of weighting values will, as in any tomographic study, to a certain degree influence the modeling outcomes, and generally, amplitudes are affected more significantly than spatial heterogeneity patterns.

3. Data Sets and A Priori Corrections

A number of surface wave and shear wave traveltimes databases have been published in recent years [e.g., Boschi and Becker, 2011], but to date they have neither been systematically combined nor analyzed in detail for the presence of anisotropic signal. We employ a uniquely diverse suite of data sets, consisting of cross-correlation delay times from Ritsema et al. [2011] and Gu et al. [2005], measured in windows around major and minor arc S phases, fundamental-mode surface wave dispersion measurements by Ekström [2011], overtone surface wave dispersion by Ritsema et al. [2004], and fundamental-mode and overtones by Visser et al. [2008a]. A complete overview of the databases employed in this study is given in Tables 1 and 2. In our final model, we chose not to include major arc data, due to the relative high uncertainties associated with such measurements. All of the aforementioned surface wave databases have been obtained using nonlinear waveform fitting procedures to extract quasi-linear observables (e.g., frequency-dependent phase delays) from the raw waveforms [van Heijst and Woodhouse, 1997; Ekström and Dziewonski, 1998; Lebedev and van der Hilst, 2008]. In terms of resolving capability, the use of these linearized measurements is comparable to more direct waveform inversion approaches, such as the nonlinear asymptotic coupling theory-based approach of the Berkeley group [Li and Romanowicz, 1996] or the

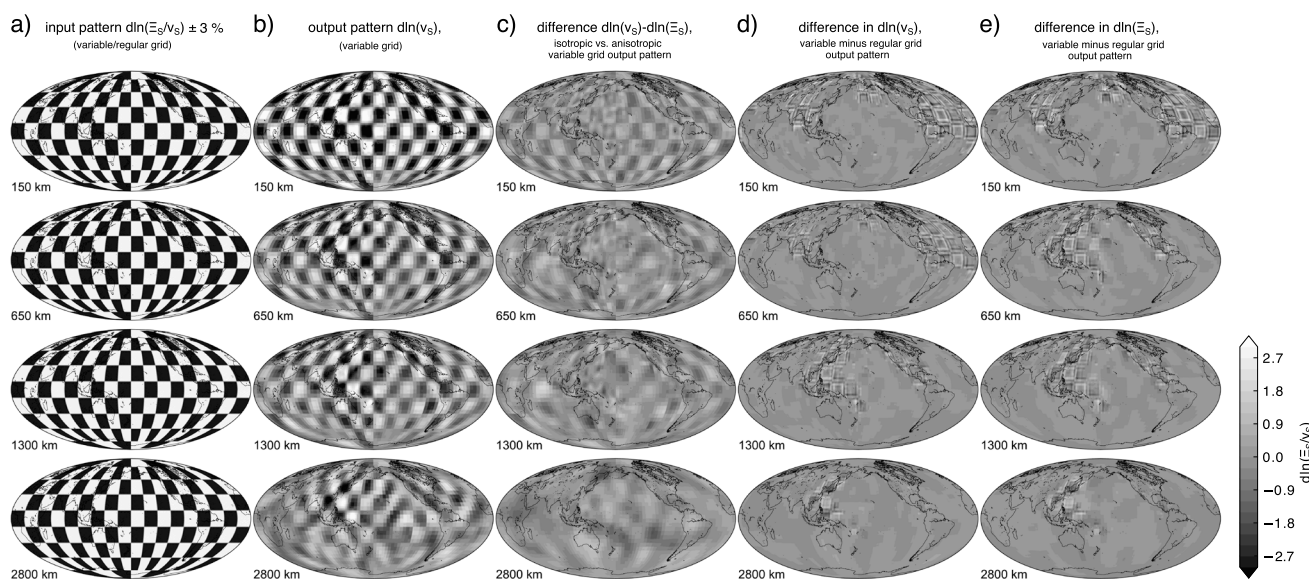


Figure 3. Resolution analysis based on the input model shown in Figure 3a. We assume a checkerboard pattern with $20^\circ \times 20^\circ$ patches having only horizontal velocity variations of 3%, on both the isotropic and the anisotropic components. Figure 3b shows the isotropic output checkerboard pattern, and Figure 3c shows the difference between the isotropic and the anisotropic output checkerboard pattern. Figures 3d and 3e show the difference between variable and regular-grid checkerboard outputs. Variable grids can better recover high frequency variations, predominantly but not limited to the high resolution parts of the grid.

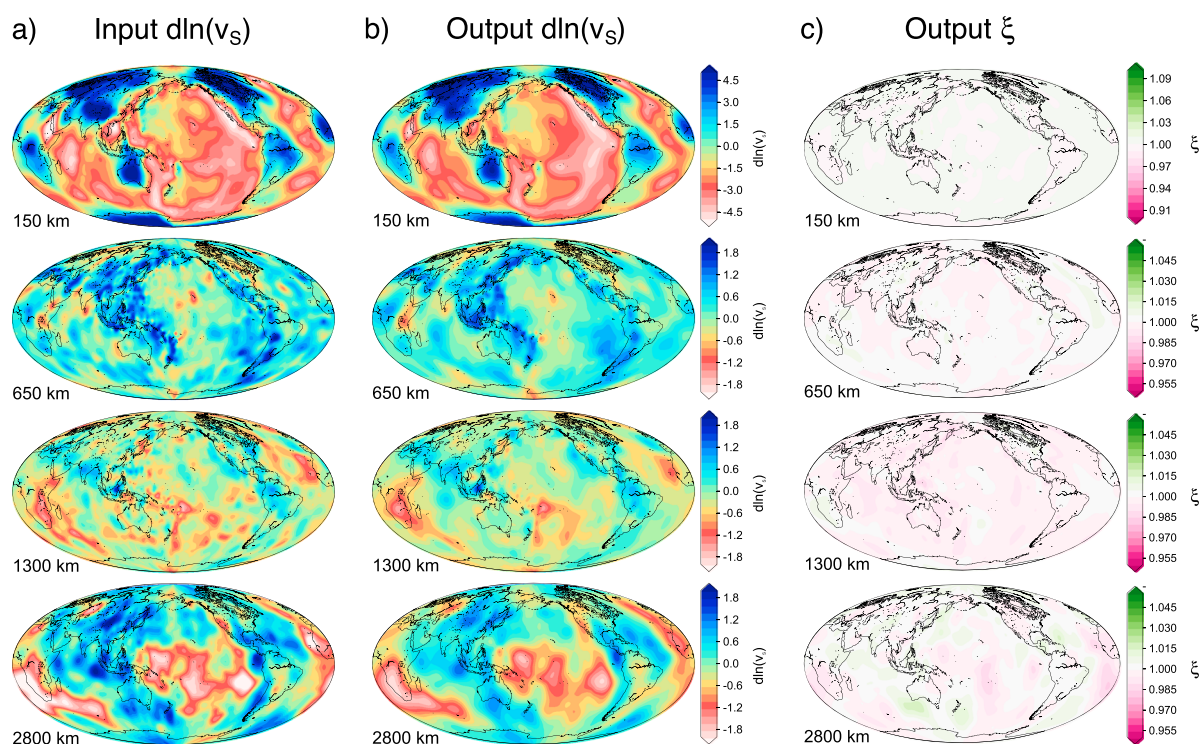


Figure 4. Trade-offs between the isotropic and the anisotropic component, investigated by using *savani* as input model for a synthetic test with noise but setting anisotropic component to zero. There is leakage between the inversion parameters, which is, however, smaller than the observed signal in ξ . Color scales are the same as in Figures 9 and 11, respectively. At lowermost mantle depths, trade-off is most significant.

partitioned waveform inversion of *Nolet* [1990]. The main advantage of including overtone information in the form of linearized phase delay measurements is that such observables can easily be given higher weights in the inversion [e.g., *Dziewoński and Romanowicz*, 2007; *Ritsema et al.*, 2011] and can be corrected for a priori crustal heterogeneity in the exact same way as it is done for the fundamental-mode portion of the data set. Correcting waveform data for crustal structure is significantly more involved [e.g., *Lekić et al.*, 2010; *Kustowski et al.*, 2007].

3.1. Crustal Correction

Surface waves are strongly influenced by the heterogeneous lithosphere, and several authors have shown that unmodeled crustal effects significantly trade off with anisotropic structure [e.g., *Bozdog and Trampert*, 2008; *Ferreira et al.*, 2010; *Panning et al.*, 2010; *Lekić et al.*, 2010]. Few authors attempt to jointly invert for crustal and mantle structure by augmenting their database with very short period (<25 s) surface wave group velocity dispersion [e.g., *Schaeffer and Lebedev*, 2013; *Lekić and Romanowicz*, 2011; *French et al.*, 2013]. In particular, *Lekić and Romanowicz* [2011] employ a smooth (or homogenized) a priori crustal model with a fixed Moho depth and additionally allow for perturbations to crustal radial anisotropy, which partly absorbs unmodeled effects due to fine-scale crustal structure. Here we follow the approach of *Boschi and Ekström* [2002] or *Nettles and Dziewoński* [2008] and use a 3-D reference model, consisting of CRUST2.0 [*Bassin et al.*, 2000] above and anisotropic PREM [*Dziewoński and Anderson*, 1981] below the Moho, to compute regionalized 1-D sensitivity functions that implicitly account for 3-D crustal variations. By integrating local phase shifts along the great-circle paths, we derive frequency-dependent corrections, which we add to our phase delay measurements. Our approach accounts for the influence of crustal structure on the sensitivity kernels. Though CRUST2.0 has some deficiencies [*Lekić and Romanowicz*, 2011], we judge it to be sufficient for our purposes. Thus, we do not attempt to invert for crustal structure itself by adding group velocity dispersion and stepwise updating our 3-D crustal model in successive iterations and set sensitivities to zero above the Moho. A similar approach has been used for example by *Nettles and Dziewoński* [2008] and *Ferreira et al.* [2010], while other authors account for crustal structure only in a path-averaged sense [e.g., *Kustowski et al.*,

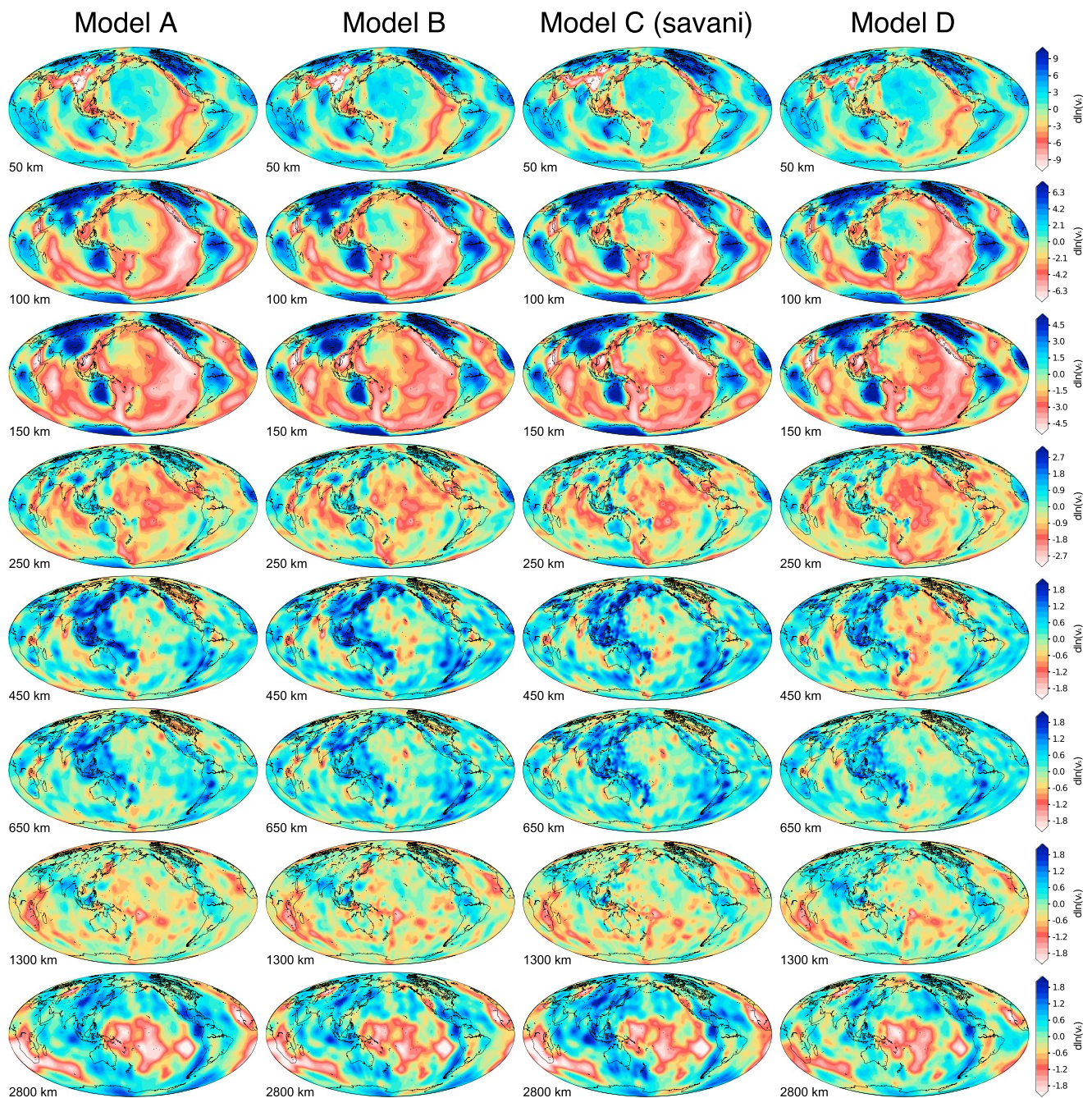


Figure 5. Isotropic v_s variations shown at the indicated depths for models A–D. Model C is our preferred model.

2008]. We also explore the effect the recently published, refined CRUST1.0 model (Appendix A) and find that the patterns of the heterogeneities that are discussed here change very little.

3.2. Azimuthal Anisotropy Correction

Upper mantle azimuthal anisotropy is reported in P_n wave observations as well as fundamental-mode Rayleigh waves [e.g., Ekström, 2011; Lebedev and van der Hilst, 2008; Debayle and Ricard, 2012]. When making the assumption of transverse isotropy, one effectively neglects any anisotropic variations perpendicular to the vertical axis of symmetry [Montagner and Nataf, 1986]. As mentioned above, it is often assumed that azimuthal coverage is sufficiently uniform for azimuthal anisotropy to average out; this assumption might be inadequate at geographic locations where raypaths exhibit a strong azimuthal preference, as for example, underneath the Pacific [Ekström, 2011]. Therefore, we attempt to correct for such azimuthal wave speed

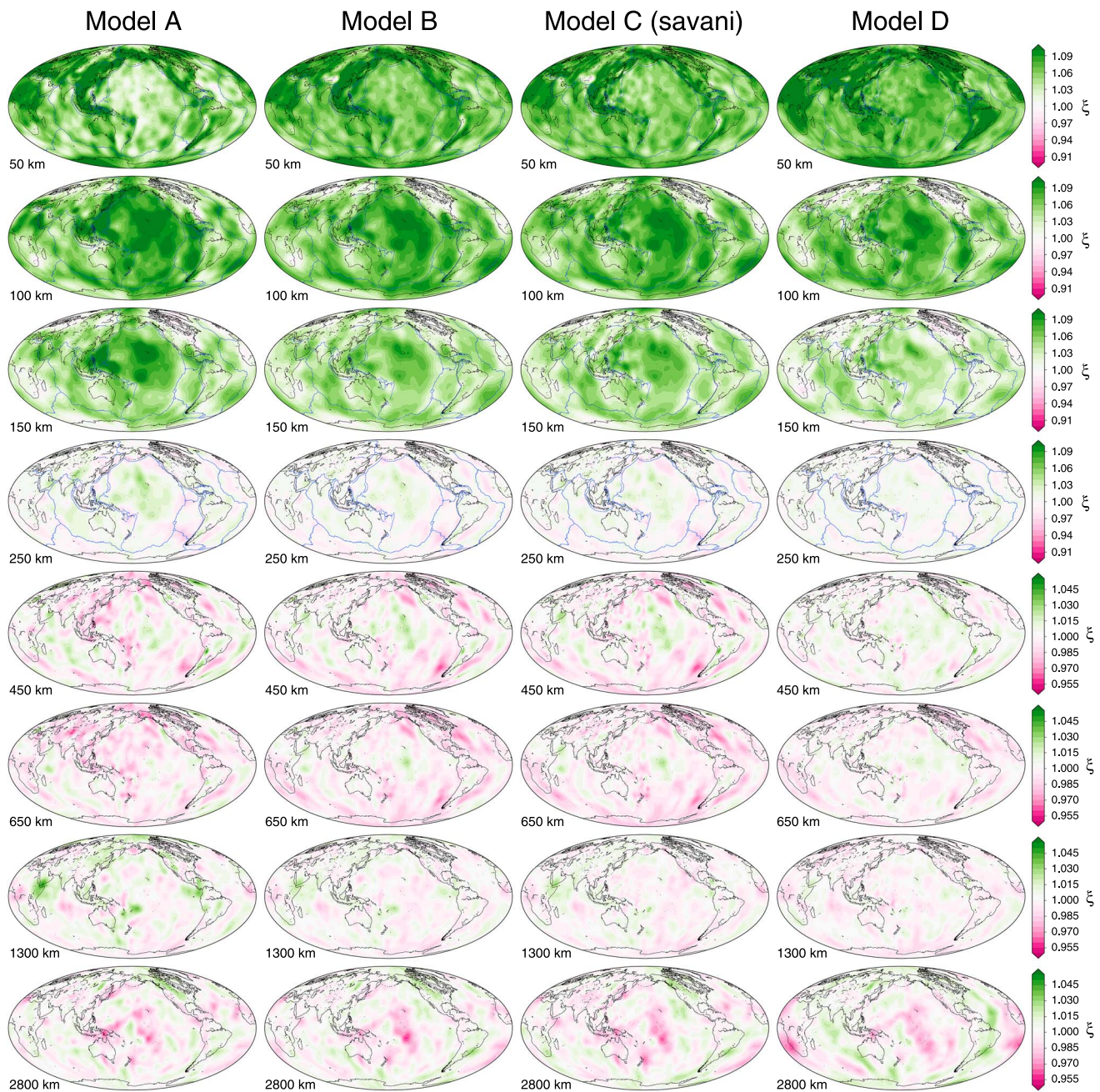


Figure 6. Variations in radial anisotropy ($\xi = (v_{SH}/v_{SV})^2$) for models A–D. Model C is our preferred model.

variations in the data, by applying ray-theoretical corrections based on the global dispersion model GDM52 [Ekström, 2011]. Love- and overtone-based models of azimuthal anisotropy are usually accompanied by large uncertainties, and we decided to only correct fundamental-mode Rayleigh wave dispersion. A description of how such corrections influence the upper mantle anisotropic variations in our model are given in section 5.2.

4. Resolution Analysis

We evaluate the resolution that can be achieved by our inversion through a checkerboard test based on the forward implementation of equation (3). This approach neglects any deficiency in the forward theory and thus underestimates the total error in the inversion [e.g., Sambridge and Mosegaard, 2002]. It is, however,

Table 3. Summary of Model Types (Models A–D) and Their Differences^a

Model Name	A	B	C (<i>Savani</i>)	D
Parameterized	v_{SH}, v_{SV}	v_S, Ξ_S	v_S, Ξ_S	v_S, Ξ_S
Adaptive	No	No	Yes	Yes
Data sets	E, V, R	E, V, R	E, V, R	E, V, R, H, G

^aData sets are abbreviated as follows: E = *Ekström* [2011], V = *Visser et al.* [2008a], R = *Ritsema et al.* [2011], H = *Ritsema et al.* [2004], and G = *Gu et al.* [2005].

equivalent to tomographic filtering [*Ritsema et al.*, 2007] applied to selected checkerboard and geodynamic models.

4.1. Checkerboard Tests

We start with a $20^\circ \times 20^\circ$, vertically constant checkerboard pattern, projected onto regular grid and adaptive grid versions of our parameterization. Both the isotropic and the anisotropic component comprise velocity variations of $\pm 3\%$. The

source station coverage to be tested is obtained by combining the data sets of *Ritsema et al.* [2011], *Ekström* [2011], and *Visser et al.* [2008a]. We add Gaussian noise with a standard deviation of 3 s [*Della Mora et al.*, 2011] to the data, before inverting it using the same regularization parameters that we use for our final models B and C (see below).

As expected, we observe that anisotropic resolution is overall lower than resolution for the isotropic component. In Figure 3d we show the output pattern of a variable grid inversion minus the one of a regular grid inversion. It can be seen that using a variable grid has some effect on the amplitudes of the recovered anomalies, and especially in areas of high resolution, one can observe that sharp contrasts are significantly better reconstructed when using an adaptive grid approach.

4.2. Trade-Offs Between Isotropic and Anisotropic Model Parameters

Since checkerboard tests depend heavily on the complexity of the synthetic input model, which may not necessarily be representative of Earth structure, we perform an additional analysis, using the output of a real data inversion as the input of a synthetic test. Following *Panning et al.* [2010] and *Kustowski et al.* [2008], we set the anisotropic component of this model to be zero everywhere and investigate leakage (i.e., parameter trade-offs) from the isotropic to the anisotropic component. As can be seen in Figure 4, the input model is well reconstructed, with little leakage from the isotropic to the anisotropic component over most of the mantle. Near the core-mantle boundary, however, we observe some trade-offs, close to where strong isotropic velocity variations are located. We infer that tomographic images of lowermost mantle anisotropy, including those presented in the following, should be treated with caution [cf. *Kustowski et al.*, 2008].

5. Model Results

We first present four alternative solutions that we derived (models A, B, C, and D), amongst which we select our final mantle model *savani* (model C). Horizontal sections through those four models are shown in Figures 5 and 6. Models A, B, and C are based on the fundamental-mode data of *Ekström* [2011], the overtone data of *Visser et al.* [2008a], and the body wave data of *Ritsema et al.* [2011] only, while model D is based on the complete data set (Tables 1 and 2). Model A is obtained by inverting directly for vertically and horizontally polarized shear wave velocities v_{SH} and v_{SV} , while models B, C, and D are parameterized in terms of average isotropic (v_S) and anisotropic (Ξ_S) variations. Models A and B are uniformly parameterized, while models C and D comprise a spatially varying inversion grid. A detailed discussion of geologic structure observed in our final Model C (*savani*) is given in section 6. A summary of the differences between models A–D is given in Table 3.

5.1. Data Fit Achieved by the Models

We examine with the help of Figure 7 the variance reductions associated with models A through D. The performance of models A through D is rather similar, despite the change in the number of free parameters: Models A and B are parameterized in terms of 1×10^5 voxels of approximately equal surface area, while models C and D include about twice as many adaptive voxels. We tune the relative weights of different data subsets such that body wave data (which are less numerous, and to which we therefore assign a higher weight) are fit about as well as surface wave fundamental modes. Fundamental modes are fit better than overtones, and data fit decreases with growing overtone number: Overtone measurements are more difficult to make, and hence less reliable than fundamental-mode ones. This effect worsens for growing overtone number.

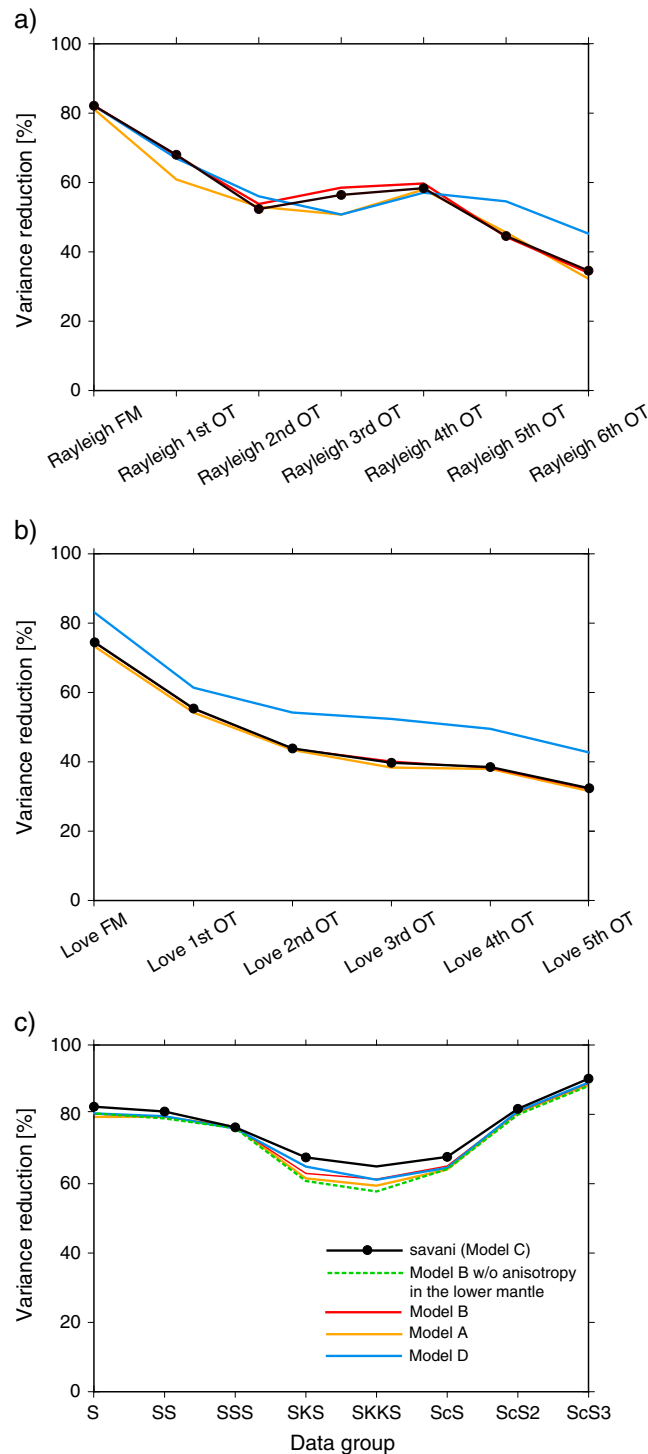


Figure 7. Grouped variance reductions for models A–D (see section 5.1). Body wave variance reductions associated with model C are highest (black lines). Preventing anisotropic variations in the lowermost mantle (yellow line) leads to slightly lower variance reductions in the lowermost mantle.

based on (i) subjective visual appraisal of the geological plausibility of cross sections and maps and (ii) the balance between model roughness and data fit, i.e., the L curve analysis [Hansen, 1992]. We evaluate two different existing approaches to anisotropy tomography, i.e., (i) parameterization in terms of v_{SH} , v_{SV} and (ii)

When directly comparing against variance reductions reported in Kustowski et al. [2008, Figure 11], one can observe a fair agreement in surface wave fundamental-mode VR of ~80%. For body waves, however, variance reduction is significantly higher for our model *savani* with direct S observations achieving a variance reduction of ~80%, compared to ~45% for model *s362wmani*. This could be explained by higher quality of our model and/or the data we inverted with respect to the study of Kustowski et al. [2008].

Since the four models compose of different subsets of the data, different numbers of free parameters and different regularization (which will all modify the data misfit in a complex way), it is not possible to entirely base preference for one model over the other on variance reduction. Geological plausibility of the resulting model remains of importance in selecting the final model. Nevertheless, the adaptive grid models C and D fit the data almost always better than the uniform grid models A and B. Model C achieves the best fit of all body wave phases, and, in particular, of SKS and SKKS, which are most sensitive to v_{SV} in the D'' region. Model D exhibits significantly higher variance reductions for all Love wave branches but fits body waves worse than model C.

To test the need for lowermost mantle anisotropy to fit the data, we have conducted one inversion, parameterized as model B, but with Ξ_5 much more strongly damped to obtain a solution with isotropic lower mantle. While the fit to other shear wave phases is unperturbed, variance reduction of SKS and SKKS data decreases by a significant ~5% (compare the yellow and red curves in Figure 7c). This suggests that, while resolution is severely limited (section 4.2), radial anisotropy can indeed be imaged with long period body wave tomography.

5.2. Model Selection

We select a preferred model among A–D based on (i) subjective visual appraisal of the geological plausibility of cross sections and maps and (ii) the balance between model roughness and data fit, i.e., the L curve analysis [Hansen, 1992]. We evaluate two different existing approaches to anisotropy tomography, i.e., (i) parameterization in terms of v_{SH} , v_{SV} and (ii)

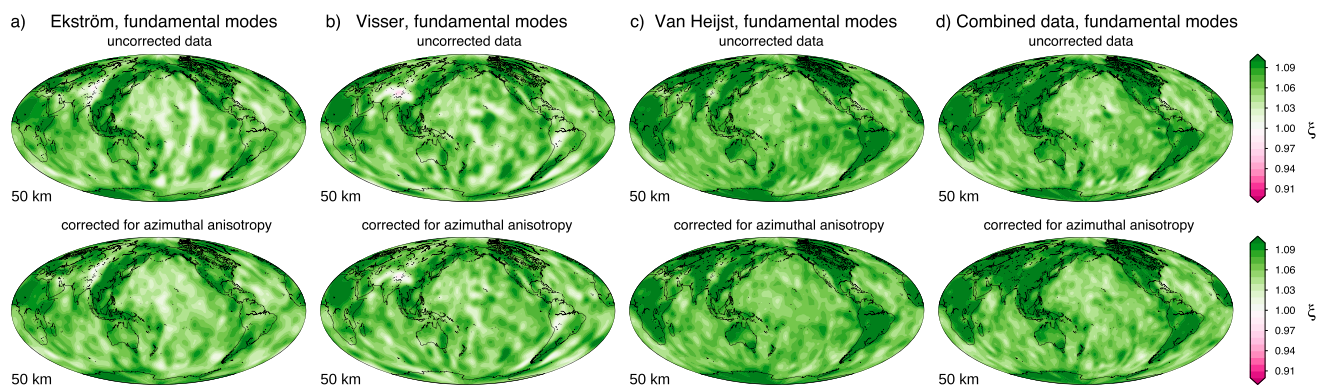


Figure 8. Anisotropic variations at a depth of 50 km, (a–d, top) before and (a–d, bottom) after correcting fundamental modes for azimuthal anisotropy. The corrections have profound effects [Ekström, 2011] and seem to remove a number of spurious anomalies such as the streak-like feature extending from Tasmania toward the East Pacific Rise (Ekström data set). Combining all data sets sharpens the continental signature at shallow depths.

in terms of v_s and ξ . In the case of separate inversions for v_{SH} and v_{SV} we impose an additional regularization constraint, minimizing their difference, assigning to the corresponding damping parameter a value similar to that of the others.

Because approach (i) requires that anisotropy ξ be determined after the inversion, combining the independently inverted v_{SH} and v_{SV} , ξ is characterized by a strong high spatial frequency signal that is probably spurious, particularly in the lower mantle [cf. Nettles and Dziewoński, 2008]. Models parameterized in terms of v_s and Ξ_s (i.e., models B, C, and D) are characterized by less small-scale variability in anisotropic amplitudes, and we infer that approach (ii) is preferable to approach (i) as used in model A. This can be seen close to the Southeast Asian subduction zones, in horizontal slices at a depth of 650 km, where model A exhibits significantly more structure than model B (Figure 6).

In Figure 8 we show anisotropic variations at a depth of 50 km, before (Figures 8a–8d, top) and after (Figures 8a–8d, bottom) correcting fundamental modes for azimuthal anisotropy. The corrections have profound effects, and remove a number of anomalies such as a streak-like feature extending from Tasmania toward the East Pacific Rise (Figure 8a, Ekström data set) [Ekström, 2011]. Combining all data sets sharpen the ocean-continent signature at shallow depths (Figure 8d).

Unlike for models A, B, and C we have not fully explored the L curve associated with model D, due to the larger computational cost of the associated inversions: the full database includes tens of millions of measurements and results (in the LSQR approach) in matrices up to 200 GB. We select model C (“savani” hereafter) as our preferred model. Model C achieves on average a better data fit than all other models. While it does not include “all” available data as model D, it does include all types of data, so that maximum possible “diversity” of the inverted data set is guaranteed.

6. Model Discussion and Comparison

We attempt to identify meaningful features in our model by comparing it against other tomographic models and geological information. We base our processing, plotting, and comparison on the spherical harmonic-based format of Becker and Boschi [2002]. Thus, all map views, cross sections, radial profiles, and power spectra are based on spherical harmonic expansions. In order to capture the finest details that are potentially resolved in the more recent tomography results, we expand such models (*sl2013sv*, *semum2*, *s40rts*, *gypsum*, *saw642anb*, *s362wmani*, and *ngrand*) up to a spherical harmonic degree of 60. Becker and Boschi [2002] indicate that this will not introduce significant spurious power. We use unity-norm real-valued spherical harmonics [e.g., Dahlen and Tromp, 1998] to express velocity variations with respect to a reference model $d \ln(v_s)$ or ξ at a certain location in space in its spherical harmonic expansion up to a maximum degree l , using the expression

$$\delta v(\theta, \phi) \approx \sum_{l=0}^{l_{\max}} [a_{l0} X_{l0}(\theta) + \sqrt{2} \sum_{m=1}^l X_{lm}(\theta) \times (a_{lm} \cos m\phi + b_{lm} \sin m\phi)] \quad (6)$$

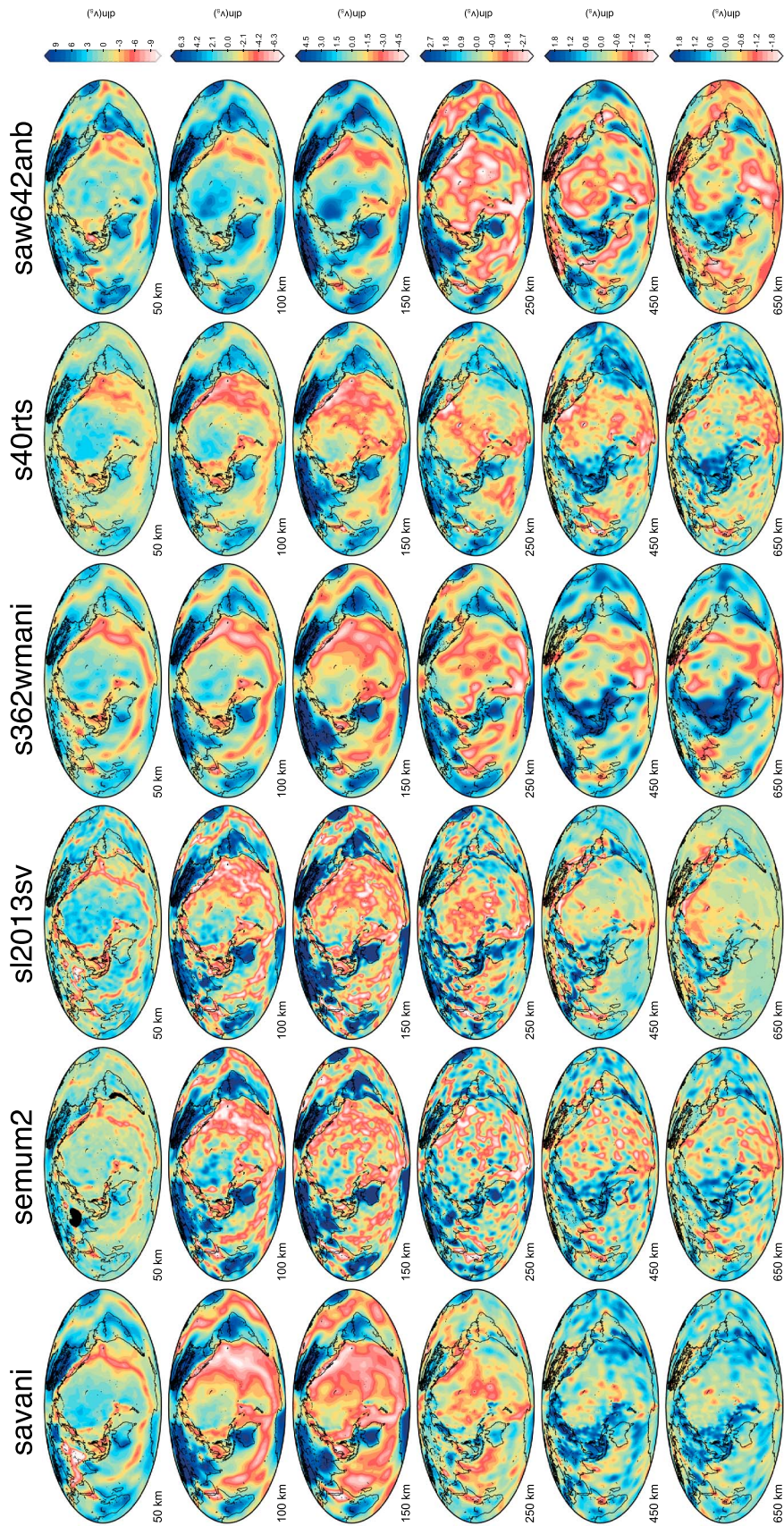


Figure 9. Upper mantle comparison between this study (*savani*) and a number of recently published upper mantle (*semum2* and *sl2013sv*) [French et al., 2013; Schaeffer and Lebedev, 2013] and whole-mantle models (*s362wmani*, *s40rts*, and *saw642anb*) [Kustowski et al., 2008; Ritsema et al., 2011; Panning et al., 2010]. Parts of *semum2* that are located within its crustal model are not interpretable and masked in black. The map views of *s40rts* and *sl2013sv* show v_{sv} , while the other models show Voigt average v_s .

where X_{lm} are normalized Legendre functions. We define the power spectrum of a tomographic model as

$$\sigma_l^2 = \frac{1}{2l+1} \sum_{m=0}^l (a_{lm}^2 + b_{lm}^2) \quad (7)$$

[see *Dahlen and Tromp*, 1998, B8]. Correlation at degree l between two models described by harmonic coefficients a_{lm} , b_{lm} and c_{lm} , d_{lm} is given by

$$r^l = \frac{\sum_{m=0}^l (a_{lm}c_{lm} + b_{lm}d_{lm})}{\sqrt{\sum_{m=0}^l (a_{lm}^2 + b_{lm}^2)} \sqrt{\sum_{m=0}^l (c_{lm}^2 + d_{lm}^2)}}. \quad (8)$$

6.1. List of Tomographic Models

In the following we give a brief description of all tomographic models against which we compare our results:

1. The *saw642anb* [*Panning et al.*, 2010] is a whole-mantle radially anisotropic S wave velocity model, based on a large data set of surface and body waveform measurements and two-dimensional non-linear asymptotic coupling theory (NACT) waveform sensitivities [*Li and Romanowicz*, 1996]. It is parameterized in horizontal and radial splines.
2. The *s362wmani* [*Kustowski et al.*, 2008] is a whole-mantle model of radially anisotropic S wave velocity variations, based on body wave traveltimes, mantle waveforms, and fundamental-mode dispersion. It is parameterized in horizontal and radial splines.
3. The *s40rts* [*Ritsema et al.*, 2011] is an isotropic v_{SV} model derived from Rayleigh wave dispersion, body wave traveltimes and normal-mode splitting functions, and parameterized in spherical harmonics up to degree 40, and radial cubic splines.
4. The *sl2013sv* [*Schaeffer and Lebedev*, 2013] is an azimuthally anisotropic v_{SV} model of the upper mantle and the crust, built from a large quantity of Rayleigh waveforms and based on automated multimode inversion [*Lebedev and van der Hilst*, 2008]. It is parameterized in triangular knots.
5. The *semum2* [*French et al.*, 2013] is based on an updated waveform data set of *saw642anb* and includes forward modeling with a spectral element method and NACT [*Li and Romanowicz*, 1996] kernels [*Lekić and Romanowicz*, 2011]. The *semum2* is parameterized in splines and employs a more realistic crustal model than its predecessor *semum*.
6. The *nd2008* [*Nettles and Dziewoński*, 2008] is a multiresolution upper mantle model, based on the method of *Boschi and Ekström* [2002], and parameterized in splines with increased tessellation density underneath North America. Crustal correction is performed in the same fashion as in this study.
7. The *smean* [*Becker and Boschi*, 2002] is a composite model, constructed by averaging the isotropic shear wave velocity models *ngrand* [*Grand et al.*, 1997], *s20rts* [*Ritsema and van Heijst*, 2000], *sb4118* [*Bolton and Masters*, 2001], and has been shown to lead to good surface wave fits [*Qin et al.*, 2009].

6.2. Upper Mantle Isotropic Structure

Figure 9 shows a comparison of the upper mantle structure of *savani* with that of earlier upper mantle and whole-mantle models. There is good agreement between the overall heterogeneity structure of all models. In particular, models agree not only on their spatial characteristics but also in the amplitudes of their velocity variations—at least across models *savani*, *semum2*, *sl2013sv*, and *s362wmani* in the upper 150 km of the mantle. However, there are also a number of locations with significant discrepancy across the models. For example, relatively fast wave speed continental keels seem to taper out at somewhat shallower depths in *savani* than *s362wmani*.

At 250 km depth, only places which are known to exhibit exceptionally thick cratons (Tibet, Africa, and North America) show above average $d \ln(v_S) = \frac{\Delta v_S}{v_S}$ in model *savani*. Contrary, 250 km deep map views of models *saw642anb* and *s362wmani* look much more similar to their 150 km equivalents (i.e., essentially show a downward continuation of uppermost mantle features). The high-resolution models *semum2* and *sl2013sv* instead are more similar to *savani*. Besides their generally higher amplitudes, the overall heterogeneity pattern in *semum2* and *sl2013sv* (such as the absence of a continental signature in above average v_S and the emerging signal of subducted slabs in Southeast Asia and underneath the Mediterranean) is similar to that of *savani*. This may reflect the relatively finely parameterized upper mantle and the depth-variable regularization scheme, employed in *savani*, which we designed to mitigate vertical smearing issues. In the

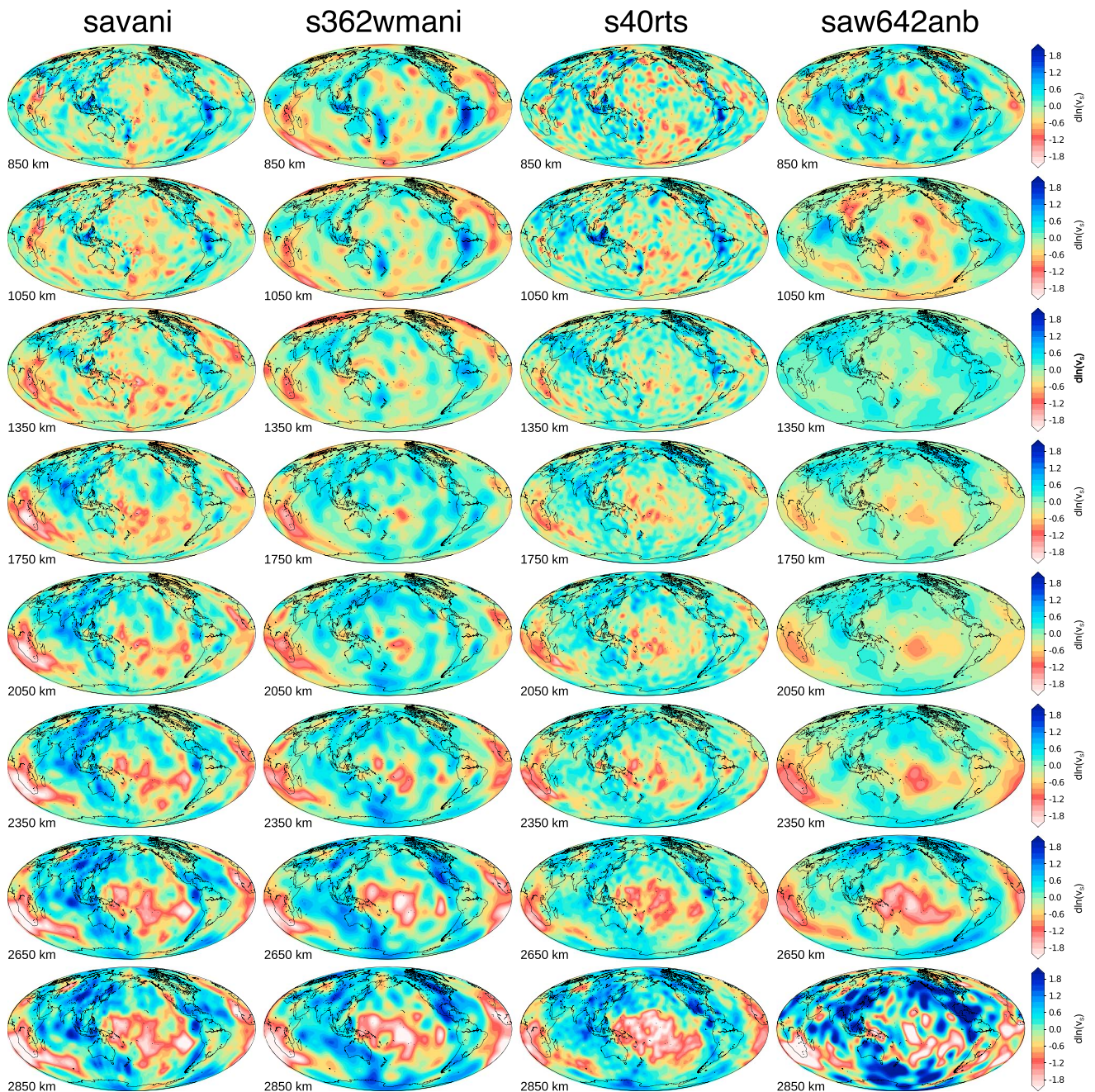


Figure 10. Lower mantle comparison between this study (*savani*) and a number of recently published whole-mantle tomographic models (*s362wmani*, *s40rts*, and *saw642anb*) [Kustowski et al., 2008; Ritsema et al., 2011; Panning et al., 2010]. The map views of *s40rts* show v_{SV} , while the other models show Voigt average v_S .

Central Pacific, the ridge signal transforms into a broader signal of low-velocity anomalies, which is at some locations clearly associated with a number of previously identified hot spots [e.g., Boschi et al., 2008].

Several models (e.g., *savani*, *semum2*, and *sl2013sv*) are characterized by a narrow channel of very low velocities at depths of around 50 km, extending from the Tibetan Plateau toward the Middle East and Eastern Europe. This structure has been recognized previously [e.g., Lekić and Romanowicz, 2011; Schaeffer and Lebedev, 2013]. Its depth extent is limited, and at ~100 km the anomaly disappears completely. The transition zone of *savani* is characterized by above average velocity anomalies underneath major subduction zones. Again, there is good agreement with *sl2013sv*, and the main difference to the other four models is

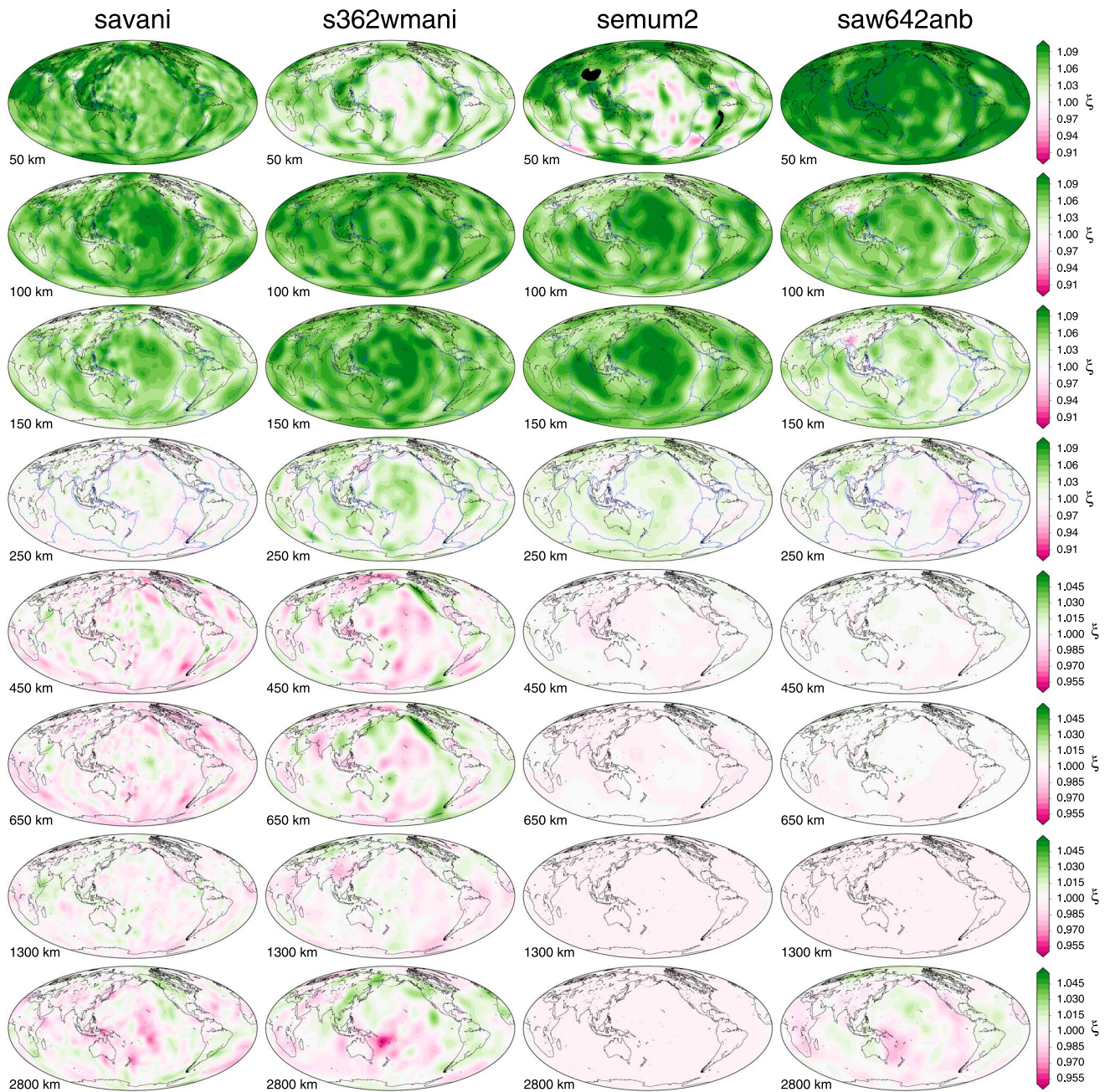


Figure 11. Comparison of the anisotropic component of *savani* with a number of previously published models (*s362wmani*, *semum2*, *saw642anb*) [Kustowski et al., 2008; French et al., 2013; Panning et al., 2010].

that we do not observe the rather strong low-velocity anomalies between the Southeast Asian and South American subduction zones in the Central Pacific.

6.3. Lower Mantle Isotropic Structure

At depths larger than 650 km (see Figure 10) the high-velocity slab signal disappears at some locations (e.g., Southeast Asia) but remains present at others (e.g., Thethys and Farallon). The *savani* seems to provide a particularly clear image of the Thethyan subduction (especially at depths shallower than 700 km) underneath the Mediterranean, which has been mapped out to relatively high detail using *P* wave tomography [e.g., Bijwaard et al., 1998; Wortel and Spakman, 2000] but was—so far—hard to constrain in global *S* wave tomography. Overall, v_s variations with respect to the 1-D reference in the lower mantle (depth ≥ 660 km) are

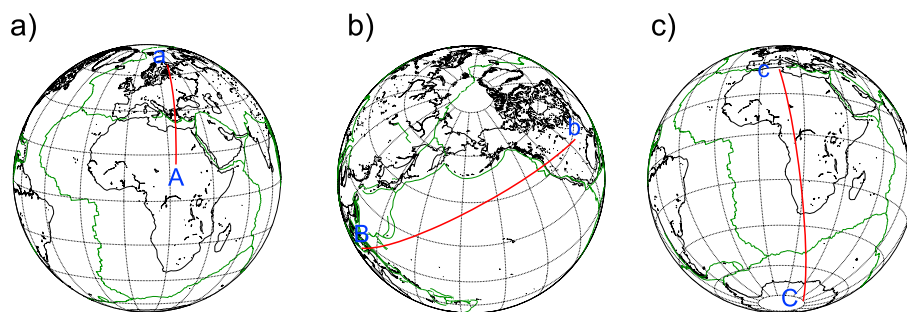


Figure 12. Geographical orientations of the profiles, depicted in Figures 13–15.

more subtle. At ~ 1800 km heterogeneity starts to increase, eventually delineating the two Large Low Shear Velocity Provinces (LLSVPs) underneath the Pacific and Africa. A noteworthy difference between *savani* and earlier models resides in the significant differences between a Western and a Southern African LLSVP. Amplitudes at the Pacific LLSVP are of the order of what has been found in earlier studies, but overall, our lower mantle comparison shows a greater variability in terms of amplitudes compared to the upper mantle. The Pacific anomaly contains slightly more intermediate-scale variability, compared to the simpler geometry of the African one. In particular, models *savani* and *s362wmani* seem to agree on a pronounced trichotomy of the lowermost mantle Pacific anomaly. Most models agree in that the African LLSVP exhibits rather sharp flanks and significantly extends from the core-mantle boundary (CMB) into the lower mantle. Some models (including *savani*) indicate a skewness of top south part of the African LLSVP toward the boundary between the African and the Antarctic Plates (see Figure 15). A number of models agree on a high v_s anomaly located underneath the Aegean, but its depth extent is poorly constrained. A similar slab structure is commonly observed in P wave tomography [e.g., *Wortel and Spakman, 2000*].

6.4. Anisotropic Structure

Figure 11 shows a comparison of the upper mantle structure of *savani* with that of a number of earlier anisotropic v_s models. As *semum2* is an upper mantle model we do not plot it below 650 km. In agreement with *Ekström and Dziewonski [1998]* and others we observe that $\xi > 1$ over a broad region underneath the

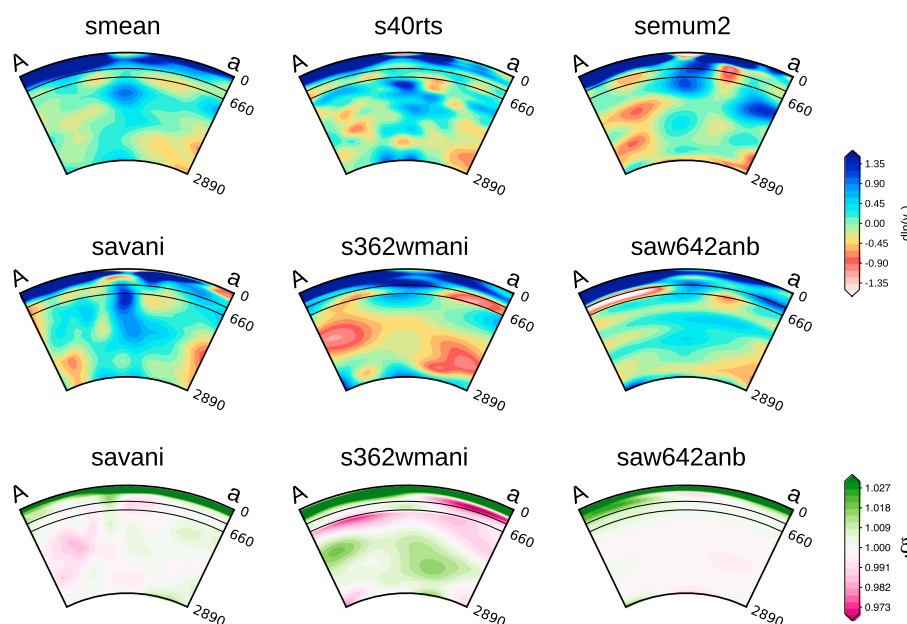


Figure 13. Vertical slices through the Thethyan subduction zone, as indicated in Figure 12a. The sections of *s40rts* and *sl2013sv* show v_{SV} , while the other models show Voigt average v_S .

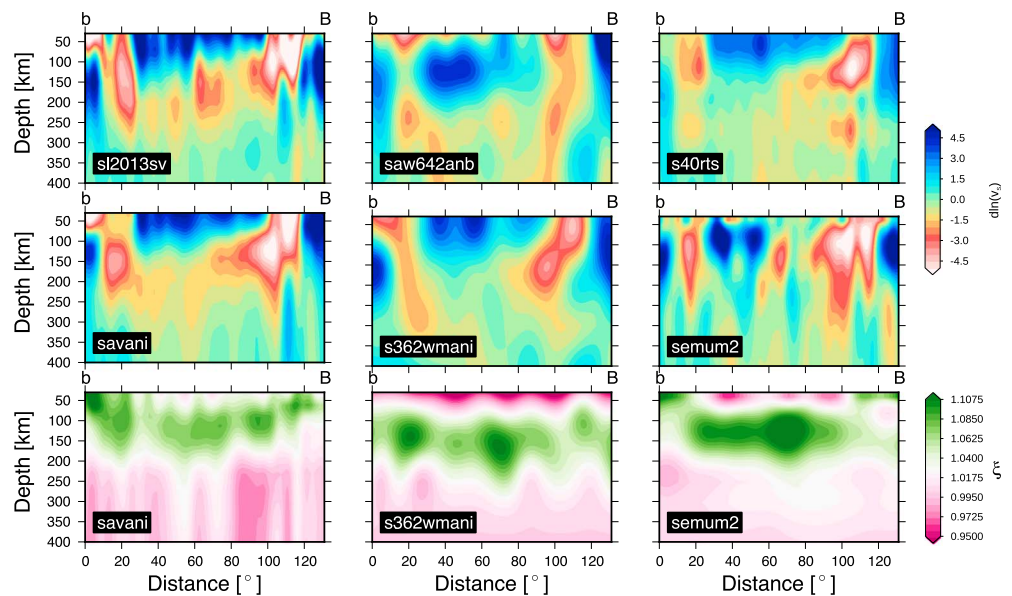


Figure 14. Vertical slices through the Central Pacific upper mantle, as indicated in Figure 12b. The sections of s40rts and sl2013sv show v_{SV} , while the other models show Voigt average v_s .

Central Pacific, but interestingly, we image the peak in $\xi > 1$ at depths of ~ 100 km, which is slightly shallower than in most other models. Note the significant depth extent of the $\xi > 1$ anomaly underneath the East Pacific Rise. At shallow depths under continents ξ is systematically stronger than underneath oceanic lithosphere. This is to some extent visible in all anisotropic models but most pronounced in *semum2*, *nd2008*, and *savani*. As discussed in more detail in section 6.11, such a continent-ocean signature may be related to frozen-in (fossil) anisotropy, stemming from previous periods of deformation that are preserved in old lithosphere. In our model we do not observe a distinct second peak in anisotropy $\xi > 1$ under continents as reported, for example, by *Gung et al.* [2003]. In the transition zone *savani* differs significantly from model *s362wmani*. While we observe a significant depth extent of the commonly observed $\xi > 1$ structure underneath the East Pacific Rise, the ridge signal seems to be reverted in *s362wmani*, showing $\xi > 1$ underneath the West Coast of the Americas. In *saw642anb*, little anisotropy is present at depths > 400 km, since the authors chose to put strong damping on anisotropic structure in the midmantle. At a number of locations, we see anomalous zones of $\xi > 1$, strictly confined by the 410 km and the 660 km seismic discontinuities (see, e.g., Figures 12–15, cross sections). In Figure 13 it can be seen that in *savani* the low-velocity anomaly increases with increasing distance from the ridge, and so does thickness of the overlying lithosphere. Overall, all models agree well with a simple half-space cooling of oceanic lithosphere. Furthermore, the amplitude and depth of the $\xi > 1$ anomaly increases toward the center of the Pacific. The lowermost mantle anisotropy as seen in *savani* is in some agreement with that of *s362wmani* and *saw642anb*, with $\xi > 1$ underneath the southwest Pacific Ocean and $\xi > 1$ under the Americas. *Kawai and Geller* [2010], for example, also find that $\xi > 1$ under the center of the Pacific using an entirely different approach and the fact that those authors use a conceptually very different method to infer radial anisotropy, is supporting the robustness of our findings. Underneath Africa, however, our results diverge from the studies of *Panning et al.* [2010] and *Kustowski et al.* [2008] in that an equivalent anomaly of $\xi > 1$ seems to be more or less absent in *savani*. This may have important consequences for our understanding of the dynamics behind the LLSVPs. Another interesting observation is the above average ξ toward the top of the African LLSVP (see Figure 15) which is present in both *savani* and *s362wmani*.

6.5. Multiscale Properties

In geodynamic applications, purely regional models quickly reach their limits since their accuracy deteriorates toward the borders of the parameterized region, and anomalies outside of the parameterized volume can be mapped into it. Purely global seismic models, however, are often of too low resolution to study the dynamics in complex tectonic settings. As described in section 2.3 *savani* is parameterized by variable-sized blocks, adapted to sampling density. The associated multiscale capabilities increase the usefulness in

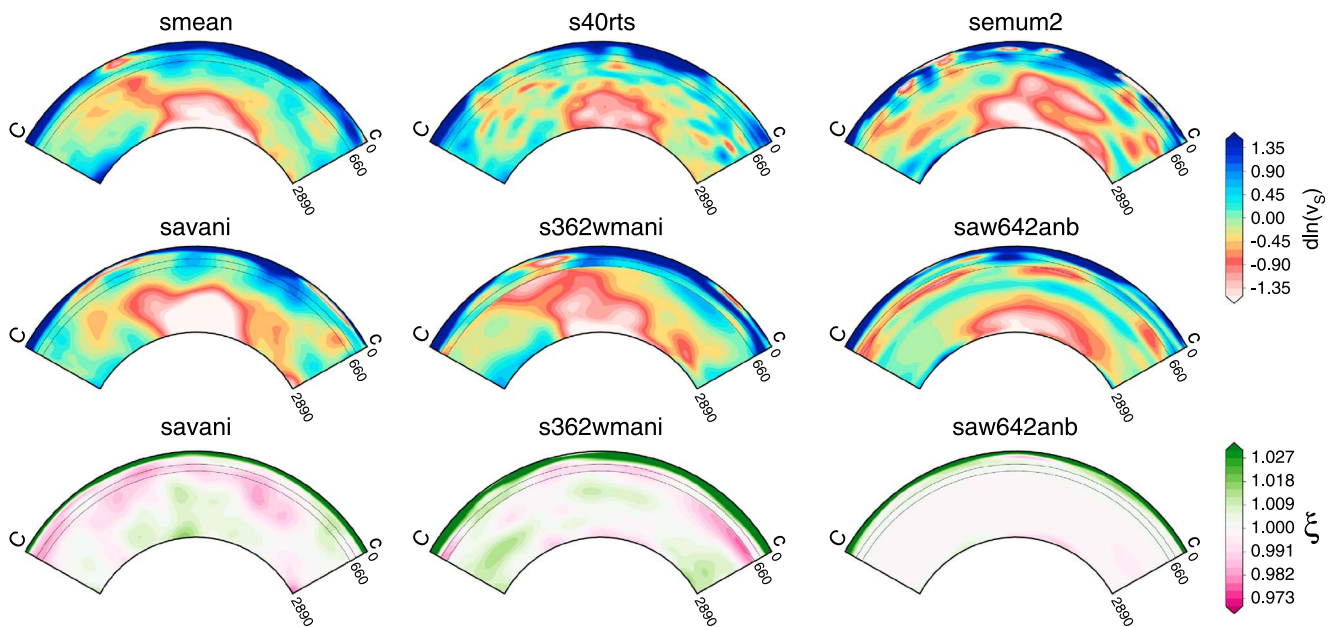


Figure 15. Vertical slice extending from Antarctica to Northern Africa, through a number of tomographic models, cutting the African LLSVP. Location of the cross section is indicated in Figure 12c. The sections of s40rts and sl2013sv show v_{SV} , while the other models show Voigt average v_S .

regional tectonic comparisons between tomography and dynamic modeling [Bijwaard *et al.*, 1998]. Examples of the resolution gain due to our parameterization approach are given in Figures 16 and 17, for Europe and South East Asia, respectively. In both figures, the middle (model B) is parameterized uniformly, while the right (model C = *savani*) is its variable grid equivalent. Clearly, there is a focusing of smaller-scale features, especially in the upper mantle, such as the low-velocity anomaly underneath Bohemian Massif (underlying the Czech Republic, southern Poland, and eastern Germany) or the Trans-European Suture Zone (extending from the Black Sea to the British Isles).

6.6. Cross Sections

We explore our model in a number of cross-section at areas of interest (see Figure 12). Figure 14 shows a vertical cross section, extending from the East Pacific Rise toward the center of the Pacific. The thickness of a fast region (presumably corresponding to the lithosphere) increases with distance from the ridge, thus being in rough agreement with half-space cooling. The isotropic low-velocity channel underneath the thickening lithosphere seems rather continuous in our model *savani*, when directly compared to models *sl2013sv* or *semum2*. Again, one can observe a slightly shallower maximum of the Pacific $\xi > 1$ anomaly, which fades away rather abruptly at a depth of ~ 200 km.

6.7. Spectral Analysis

We compare in Figure 18 the power spectra of the isotropic component of *savani* with those of *smean*, *saw642anb*, and *s362wmani*. All spectra are dominated by degree 2 at all mantle depths, but *savani* shows the most continuous $l = 2$ power with depth. At ~ 200 km there is a sharp drop in power, associated with the transition between continental lithosphere and mantle. The *savani* is characterized by a slightly shallower and sharper drop in power in the upper mantle. All models exhibit an increase in power toward the lowermost mantle. Other noteworthy observations include the weak degree 7 at all depths in the lower mantle.

The harmonic expansion of ξ leads to the spectra of Figure 19. While in *s362wmani* and *savani* degrees up to 5 dominate in the upper mantle, *saw642anb* includes also significant power at shorter wavelengths. The *savani* and *s362wmani* seem to consistently image a sharp increase in degree 1 anisotropic variations below the 660 discontinuity. The degree 1 of both *s362wmani* and *savani* jumps near the 660 km discontinuity. This is not as clear in *saw642anb*, in which the authors penalized anisotropy more strongly below the transition zone, since they did not observe a statistical improvement of data fit when allowing for anisotropy at those depths. In anisotropic (ξ) cross-model correlation plots *s362wmani* and *savani* (Figure 20) are almost entirely decorrelated (even at $l = 2$) at transition zone depths but correlate slightly better in the lower

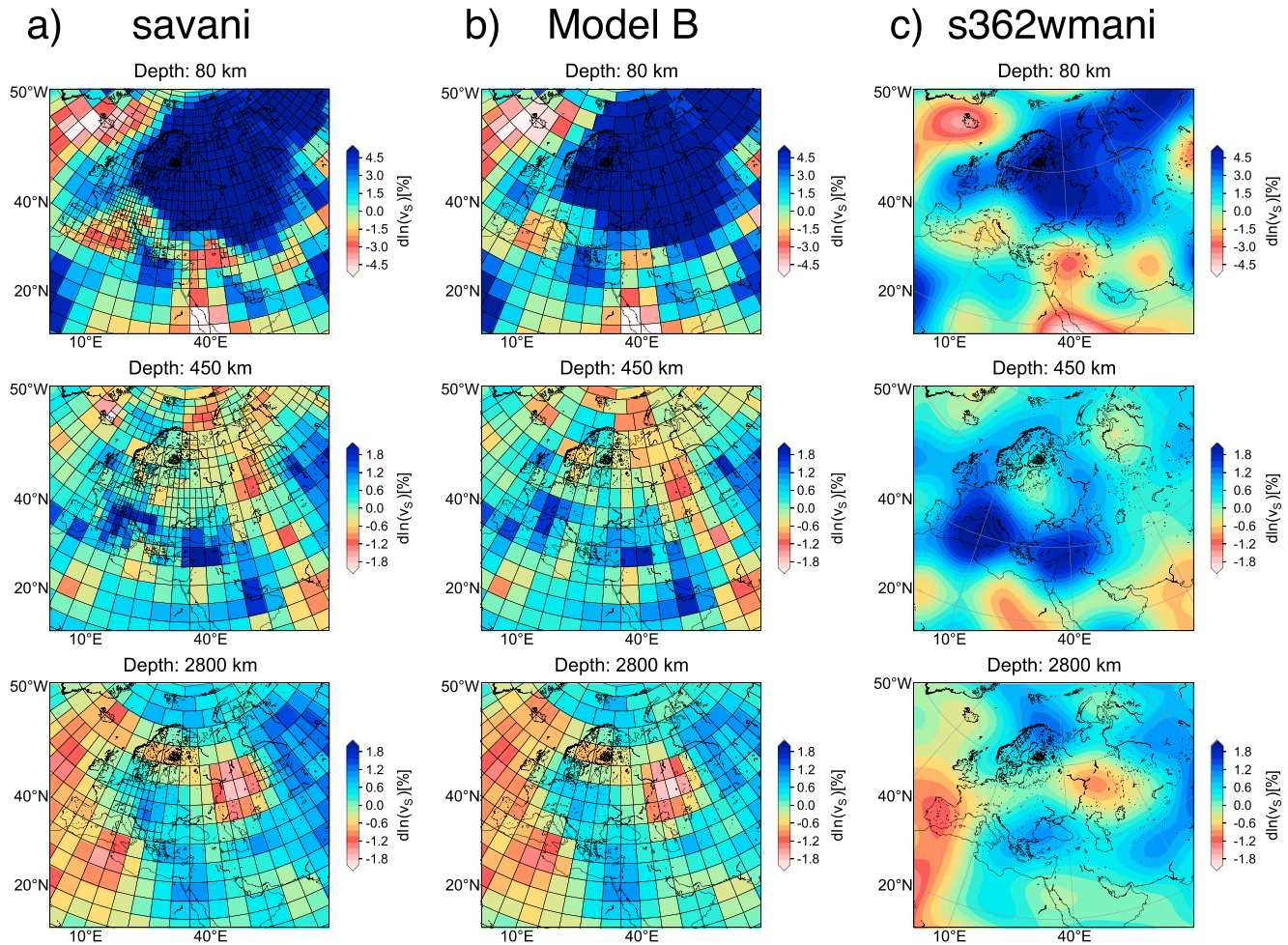


Figure 16. Zoomed horizontal sections of *savani* (model C) and model B underneath Europe. Model B is parameterized uniformly, while model C is the variable grid equivalent. One can observe a significant sharpening, especially in the upper mantle, where a number of small-scale features (e.g., the Bohemian Massif) show up when turning on the data-adaptive grid.

mantle. In the uppermost mantle, correlation in ξ is good up to $l \sim 7$. Cross correlation between *s362wmani* and *saw642anb* is slightly better at low degrees at most mantle depths but poorer in the upper and lowermost mantle.

6.8. Average Radial Profiles

Computing regionalized and global average profiles of tomographic models allows additional insights into the relation between isotropic and anisotropic variations with tectonics and surface geology. We employ the global tectonic regionalization GTR-1 by *Jordan* [1981], who subdivided the tectosphere in six oceanic and continental tectonic subunits. Three different oceanic regions are defined according to their crustal age (along the 25 and 100 Myr isochrons), while continental regions are subdivided in Precambrian shields/platforms, Phanerozoic platforms, and Phanerozoic orogens/magmatic belts. We show in Figure 21 the regional RMS (root-mean-square) v_s (top) and average ξ (bottom) profiles from *savani* and compare them to equivalent profiles obtained from other models. The *savani* exhibits a clear depth increase of the $\xi > 1$ peak underneath oceans, with increasing ocean age, similar to *nd2008*. The peak in $\xi > 1$ is found slightly shallower compared to other models.

6.8.1. Isotropic Profiles

The v_s profiles in Figure 21a are all characterized by a dichotomy between oceanic and continental regions. RMS velocity under oceans grows with increasing age. Under continents, it is much higher for all kinds of platforms, with respect to magmatic belts. Interestingly, old oceans (yellow) generally exhibit higher RMS velocities than young oceans (dark red) at shallower depths, but this is found to reverse at depths of

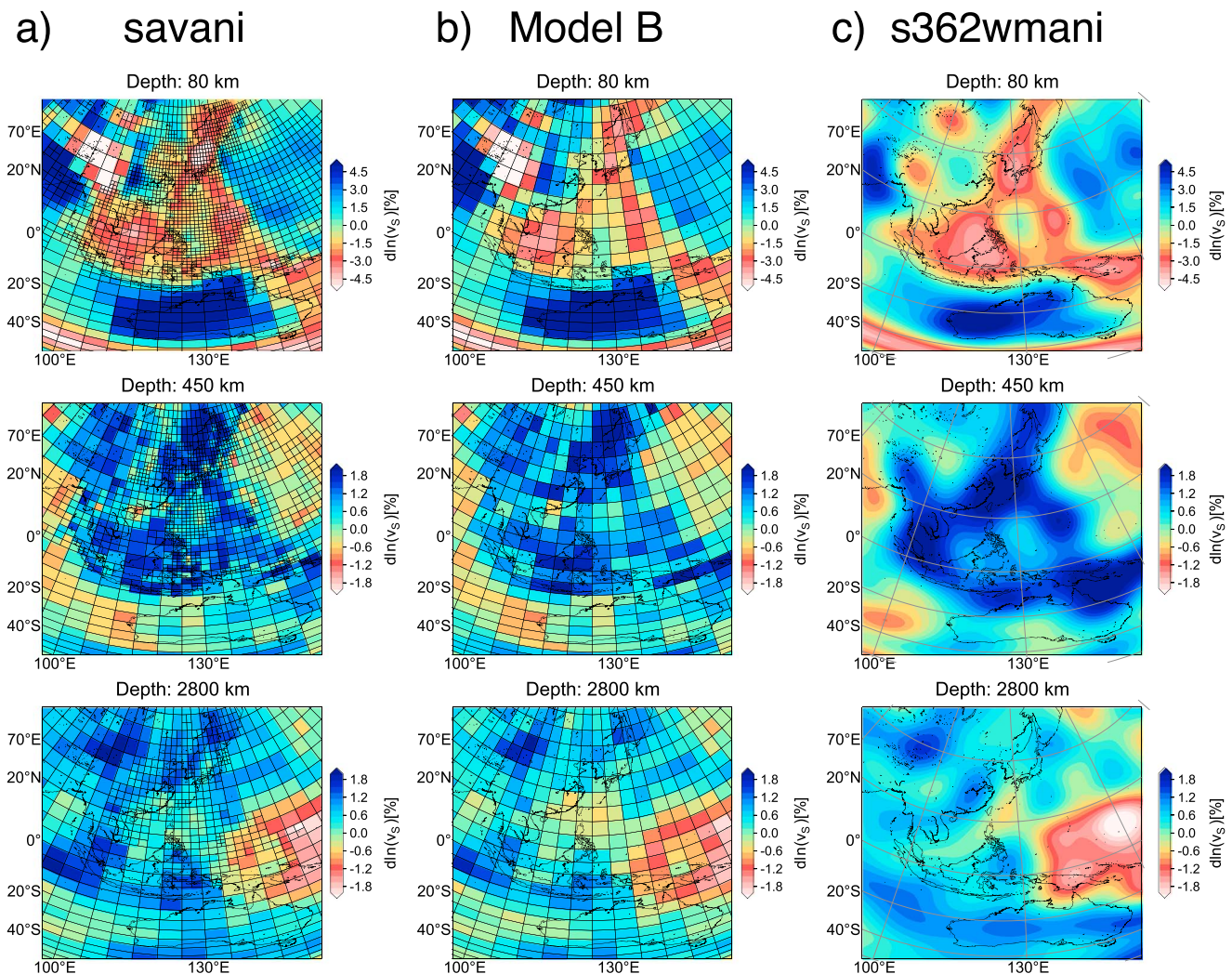


Figure 17. Zoomed horizontal sections of *savani* (model C) and model B underneath Southeast Asia. Model B is parameterized uniformly, while model C is the variable grid equivalent. There is a significant focusing of fine-scale structure. Note the good long-wavelength agreement with *s362wmani* at all mantle depths.

~70 km which is inconsistent with a purely thermal origin. Overall *savani* looks very similar to *nd2008* with our model generally showing slightly higher RMS amplitudes—especially at young oceans—at depths of ~100 km. This is likely explained by overlaps in data and the similar inversion method. A noteworthy difference between *savani* and *nd2008* is the more pronounced drop in RMS at continental regions at ~120 km depth, where *savani* is more similar to *semum2* and *sl2013sv*. The whole-mantle models *s362wmani* and *saw642anb* exhibit slightly less variability in their regional averages.

6.8.2. Anisotropic Profiles

In oceanic regions (red to yellow colors in the ξ -profiles in Figure 21b) one can notice that the depth of the maximum- ξ peak increases subtly with the age of the oceanic lithosphere. This effect is present in several models besides *savani* but is most pronounced in *nd2008*. On the contrary, average regional profiles for models *saw642anb* agree well with the PREM average at all tectonic units and do not exhibit a significant difference between continental and oceanic zones. In models *semum2*, *savani*, and *nd2008* the difference between continental and oceanic regions is most pronounced. According to both *savani* and *nd2008*, Precambrian shields (Figure 21, dark blue) are characterized by significantly larger ξ than Phanerozoic orogenic belts and platforms (Figure 21, light blue). This is plausible since old continental regions presumably have undergone longer episodes of tectonic deformation assuming those would yield preferentially horizontal alignment. The opposite is observed in models *semum2* and *saw642an*, where Precambrian shields show the lowest amplitudes in anisotropy. A difference between *savani* and other models is that the peak in $\xi > 1$ at oceanic regions shows up at relatively shallow (80–100 km) depth, compared to 110–150 km

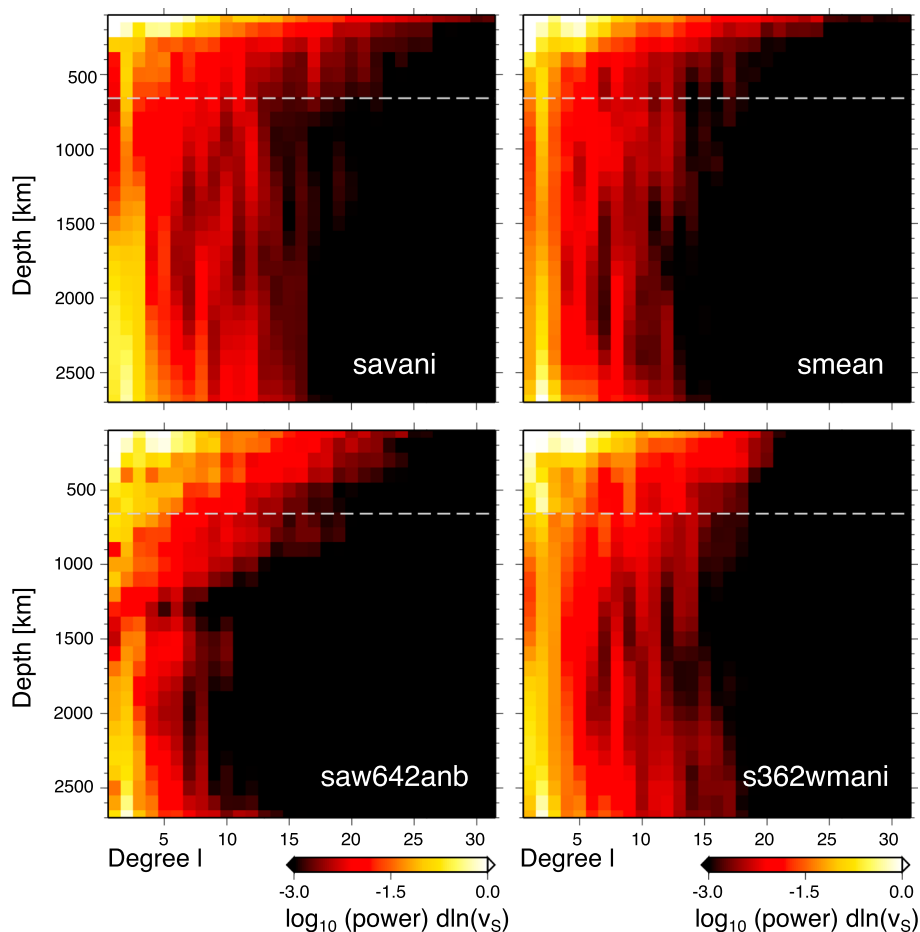


Figure 18. Spherical harmonic power spectra for the isotropic components of a number of models.

in *nd2008* and 120–160 km in *semum2*. This has implications for the origin of a possible oceanic LAB (lithosphere-asthenosphere boundary) [e.g., *Kawakatsu et al., 2009*].

6.8.3. Relation to Probabilistic Tomography

Comparisons between continental and oceanic regions were also reported in the probabilistic anisotropic tomography study of *Beghein and Trampert [2004]*. Their findings agree very well with our results, in the sense that, on average, oceanic regions seem to require positive deviations from PREM at depths between 100 and 200 km, while continental regions require negative deviations, at shallower depths [see *Beghein and Trampert, 2004, Figures 1 and 2*]. Furthermore, *Beghein and Trampert [2004]* find a small probability for

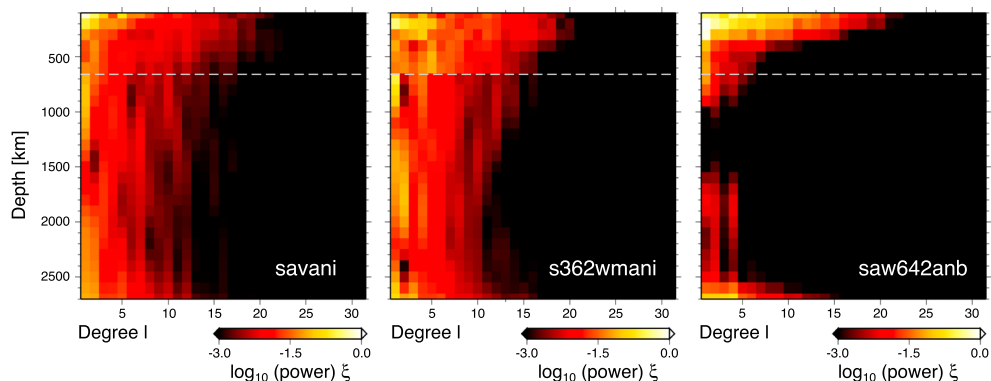


Figure 19. Spherical harmonic power spectra for the anisotropic components of a number of models.

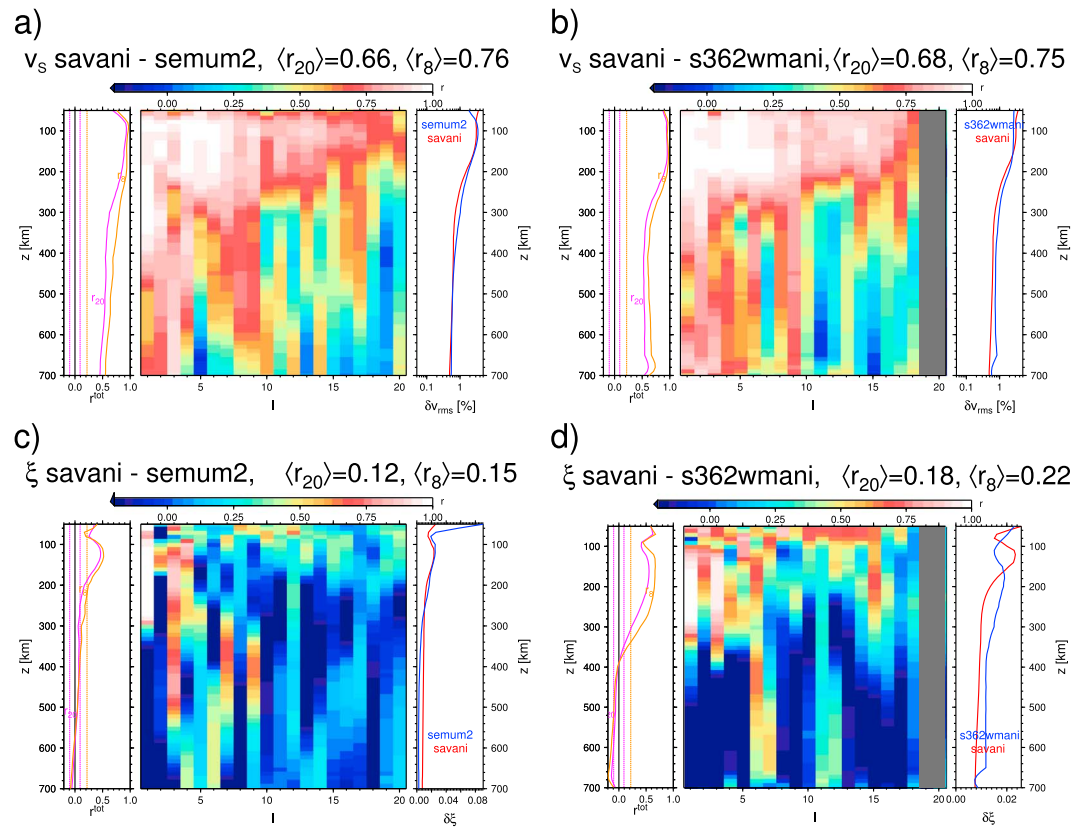


Figure 20. Cross-correlation spectra between models *s362wmani*, *semum2*, and *savani* for the parameters ξ and v_s . $\langle r_{8/20} \rangle$ is the total correlation coefficient up to degree $l = 8$ and $l = 20$, respectively. (a and c) The total correlation r_{tot} as a function of depth and (b and d) the RMS of δv_s or $\delta \xi$, respectively [Becker and Boschi, 2002]. Correlation is fair up to a spherical harmonic degree of 5 in the upper mantle and a degree of ~ 5 in the lowermost mantle but much poorer between the transition zone and ~ 2400 km.

$\xi < 1$ in the transition zone, especially underneath young oceans. A significant probability for $\xi < 1$ was in the depth range between 400 and 600 km was also found by Visser *et al.* [2008b].

6.9. Validity of Crustal Corrections

It is well known that in the case of coupling across mode branches, the validity of crustal corrections may deteriorate [e.g., Bozdag and Trampert, 2008; Ferreira *et al.*, 2010]. Bozdag and Trampert [2008] use the spectral element method to quantify the accuracy of our method, indicating that it is accurate at least down to a period of 60 s. To examine the robustness of our results we repeated our inversion excluding periods < 60 s, and found that the model does not change substantially. Predominant features, like the sudden sign change in anisotropy at a depth of ~ 100 km underneath continents and the continental signature at ~ 50 km depth, remain stable but appear somewhat less sharp. Together with the general consistency of our results with other studies that use entirely different approaches to account for the crust, we judge that anisotropic upper mantle structure in our modeling is not dominated by crustal contamination.

6.10. Anisotropy and the LAB

The idea that upper mantle radial anisotropy is, to some extent, related to shear effects in the upper mantle and the transition between the rigid lithospheric lid and the less viscous underlying asthenosphere has been around for a while [e.g., Montagner, 1998]. A number of authors have tried to employ ScS reverberations [Revenaugh and Jordan, 1991], receiver functions [Kumar and Kawakatsu, 2011], or seismic refractions [Tan and Helmerger, 2007] to detect a seismic velocity contrast of $\sim 5\text{--}15\%$ at depths between 70 and 80 km, underneath oceanic lithosphere (75 km in the Central Pacific). Schmerr [2012] use SS underside reflections and image a velocity gradient underneath the Pacific, correlated with age and distance from the upwellings. In the face of those recent estimates on LAB depth, our finding that the peak in anisotropy ($\xi > 1$ underneath oceans) may in fact be located ~ 50 km shallower compared to earlier estimates might be more consistent

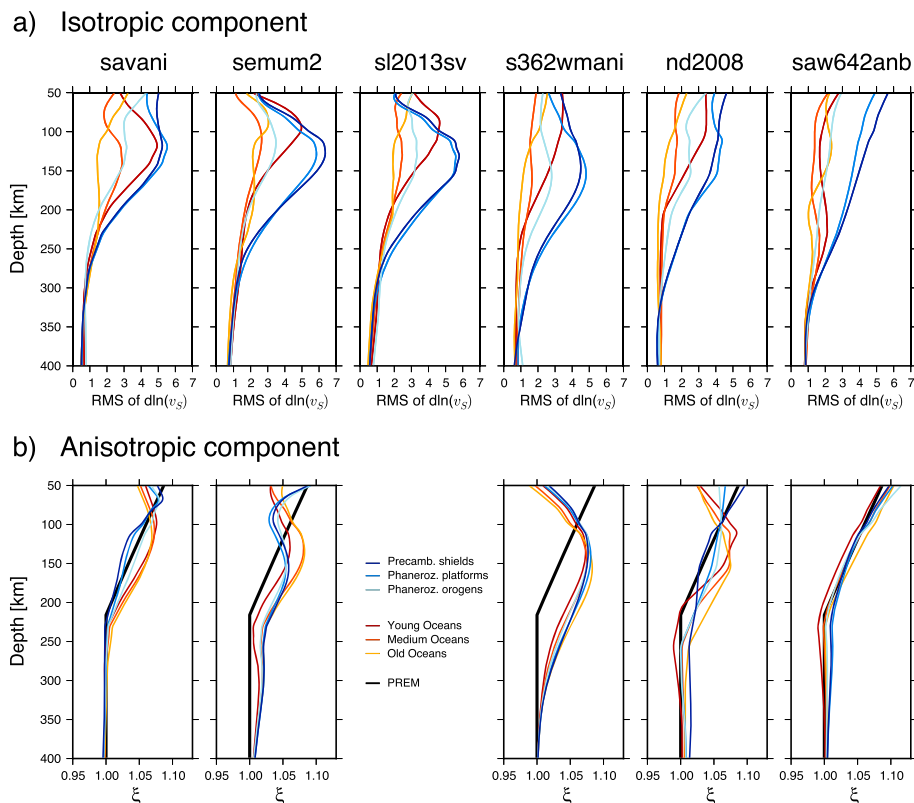


Figure 21. Tectonic regionalization based on GTR-1 of Jordan [1981] of a number of whole-mantle and upper mantle tomographic models. Dark red, red, and orange colors correspond to young, medium, and old oceanic lithosphere, while dark blue, blue, and light blue correspond to Precambrian shields/platforms, Phanerozoic platforms, and Phanerozoic orogens/magmatic belts. The black line corresponds to the radial anisotropy included in our reference model PREM.

with its interpretation as being caused by convective shearing of olivine in dislocation creep in the upper asthenosphere [Podolefsky et al., 2004; Becker et al., 2008; Behn et al., 2009]. Distinguishing between such a lattice preferred orientation-based origin of radial anisotropy and shape preferred mechanisms such as partial melting [e.g., Kawakatsu and Yoshioka, 2011] does, however, remain a challenge.

6.11. Fossil Anisotropy Underneath Continents

The difference in radial anisotropic patterns between continents and oceans (which in models *savani*, *semum2*, *nd2008*, and to a lesser extent *s362wmani* shows up in the form of above average ξ underneath continents at depths of around 50 km) points to a problem in interpretation of azimuthal anisotropy. The few existing SKS-splitting observations that are available for oceanic regions are consistent with independent seismological data sets (such as azimuthally anisotropic tomography) and can be well reconciled with geodynamic models of mantle circulation [Behn et al., 2004; Becker et al., 2007]. At continental regions, which exhibit a significantly stronger spatial variability in SKS-splitting fast axes [e.g., Silver, 1996; Fouch and Rondenay, 2006] this is generally not the case. A number of authors suggest that such discrepancies may be attributed to complex remnant (i.e., fossil or “frozen in”) anisotropy, representing a record of previous episodes of deformation which are much harder to model. Becker et al. [2007] developed a stochastic model based on a large compilation of SKS-splitting measurements and showed that such models are helpful to explain the residual between synthetic anisotropy from flow simulations and tomographic observations [Becker et al., 2008]. Our new results of strong $\xi > 1$ in the old continents is consistent with this idea and suggests that quantitative exploration of global radial anisotropy patterns should be revisited.

7. Conclusions

We inverted multiple-surface wave and body wave data sets for radially anisotropic whole-mantle shear velocity structure, using a novel multiscale tomography approach. Our new model *savani* highlights several robust features, which we consider to be as stable as their isotropic counterparts. We find distinct

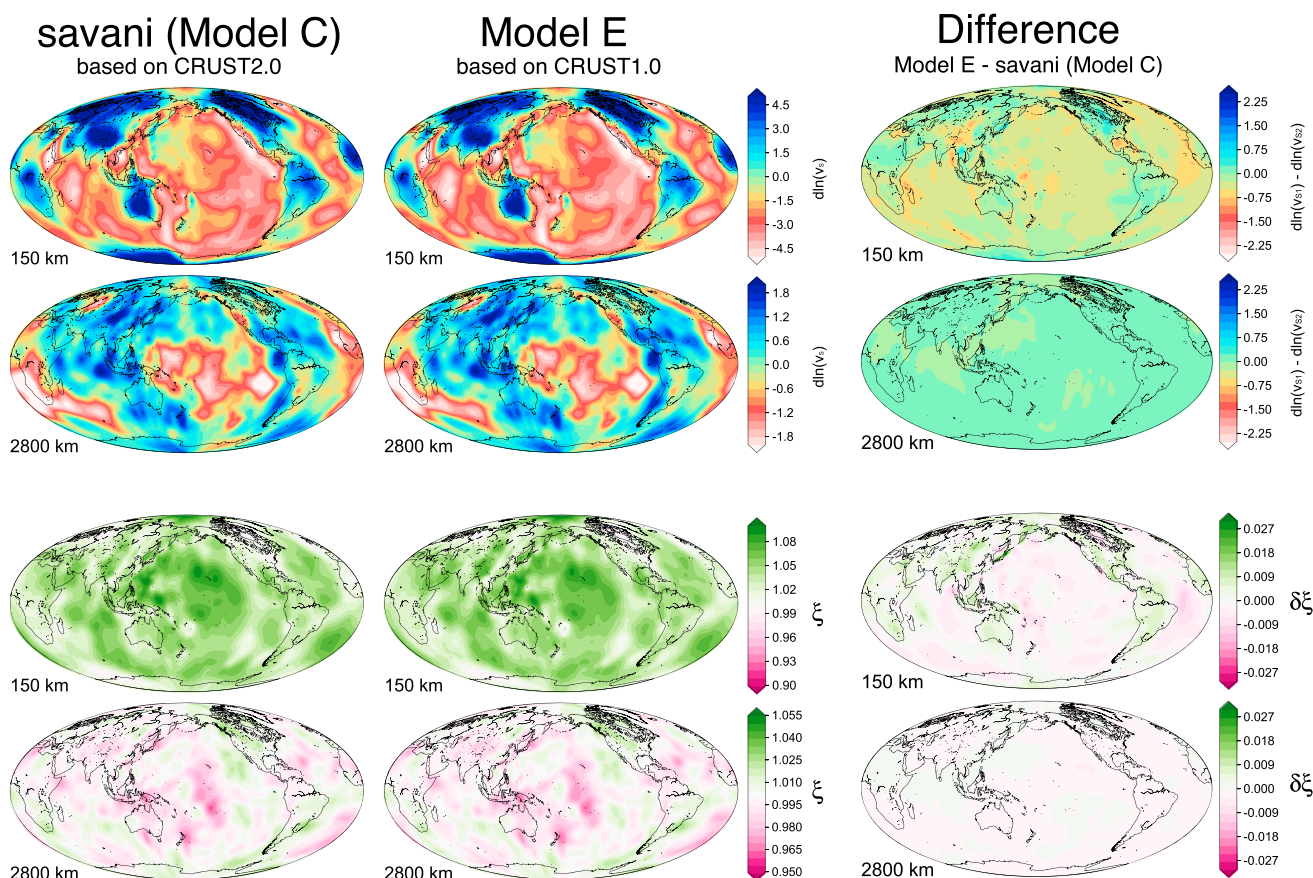


Figure A1. Map view comparison of *savani* (model C) with a preliminary test model in which the crustal model CRUST2.0 is replaced with its successor CRUST1.0.

delineation between continents and oceans in the depth range between 50 and 80 km of the anisotropic component of our model *savani*, with above average $\xi > 1$ underneath continents and below average $\xi < 1$ underneath oceans. Underneath the Central Pacific, we recover an anomaly of above average $\xi > 1$, having its maximum between 70 and 130 km, which is slightly shallower than what has been found previously, as well as $\xi < 1$ underneath the East Pacific Rise, extending down to depths of ~ 400 km. Lastly, there is an indication for $\xi < 1$ in vicinity of the Pacific LLSVP in the core-mantle boundary region. The multiscale properties of our model make it particularly suited for subsequent tomographic-geodynamic comparisons. Furthermore, *savani* can act as a useful basis in subsequent regional tomography studies. Continued efforts to map out the anisotropic velocity structure of our planet are likely to play a key role in improving our understanding of mantle dynamics.

Appendix A: A New Crustal Model

During the process of publishing this paper an update of the crustal model CRUST2.0, on which *savani* is partly based, became available. While CRUST2.0 was essentially a “regionalized” model, with ~ 350 different regions, crustal structure in the new model CRUST1.0 [Laske *et al.*, 2013] varies spatially over the entire globe, with $1^\circ \times 1^\circ$ resolution. Fully integrating CRUST1.0 in our inversion algorithm, including body wave crustal corrections obtained using the waveform approach of Ritsema *et al.* [2011], is computationally very expensive and beyond the scope of the present study. It is, however, important to verify that the main features of *savani* will not be exceedingly perturbed when updating the crust. As a preliminary test, we therefore applied a linear crustal correction based on CRUST1.0 to our surface wave (and not the body wave) data but without recomputing the local sensitivity kernels, and conducted a new inversion. Figure A1, where the result of the new inversion is dubbed “model E”, shows that this data correction does not fundamentally alter our results: While amplitudes seem to be affected slightly more, changes in heterogeneity patterns

are minor. There is no reason to expect that the discrepancy will grow when implementing a complete, nonlinear crustal correction as done here with CRUST2.0.

Acknowledgments

The authors would like to thank the various authors for making their data sets, tomographic and geological models freely available. We also acknowledge the useful comments of Sergei Lebedev and one anonymous reviewer, which helped to clarify the presentation.

References

- Anderson, D. L., and A. M. Dziewoński (1982), Upper mantle anisotropy: Evidence from free oscillations, *Geophys. J. R. Astron. Soc.*, *69*, 383–404, doi:10.1111/j.1365-246X.1982.tb04956.x.
- Anderson, O., and D. G. Isaak (1995), Elastic constants of mantle minerals at high temperature, in *A Handbook of Physical Constants: Mineral Physics and Crystallography, AGU Handbook*, vol. 2, edited by T. Ahrens, pp. 64–98, AGU, Washington, D. C.
- Babuška, V., and M. Cara (1991), *Seismic Anisotropy in the Earth*, Kluwer Acad., Dordrecht, Netherlands.
- Bassin, C., G. Laske, and G. Masters (2000), The current limits of resolution for surface wave tomography in North America, *Eos Trans. AGU*, *81*(48), Fall Meeting Suppl., Abstract S12A-03.
- Becker, T. W., and L. Boschi (2002), A comparison of tomographic and geodynamic mantle models, *Geochem. Geophys. Geosyst.*, *3*(1), 1003, doi:10.1029/2001GC000168.
- Becker, T. W., S. Chevrot, V. Schulte-Pelkum, and D. K. Blackman (2006), Statistical properties of seismic anisotropy predicted by upper mantle geodynamic models, *J. Geophys. Res.*, *111*, B08309, doi:10.1029/2005JB004095.
- Becker, T. W., J. T. Browaeys, and T. H. Jordan (2007), Stochastic analysis of shear-wave splitting length scales, *Earth Planet. Sci. Lett.*, *259*, 29–36, doi:10.1016/j.epsl.2007.05.010.
- Becker, T. W., B. Kustowski, and G. Ekström (2008), Radial seismic anisotropy as a constraint for upper mantle rheology, *Earth Planet. Sci. Lett.*, *267*, 213–237, doi:10.1016/j.epsl.2007.11.038.
- Beghein, C., and J. Trampert (2004), Lateral variations in radial anisotropy and consequences for the upper 1200 km of the mantle, *Geophys. Res. Abstr.*, *6*, 1348.
- Behn, M. D., C. P. Conrad, and P. G. Silver (2004), Detection of upper mantle flow associated with the African Superplume, *Earth Planet. Sci. Lett.*, *224*, 259–274, doi:10.1016/j.epsl.2004.05.026.
- Behn, M. D., G. Hirth, and J. R. Elsenbeck II (2009), Implications of grain size evolution on the seismic structure of the oceanic upper mantle, *Earth Planet. Sci. Lett.*, *282*, 178–189, doi:10.1016/j.epsl.2009.03.014.
- Bijwaard, H., W. Spakman, and E. Engdahl (1998), Closing the gap between regional and global travel time tomography, *J. Geophys. Res.*, *103*, 30,055–30,078.
- Bolton, H., and G. Masters (2001), Travel times of P and S from the global digital seismic networks: Implications for the relative variation of P and S velocity in the mantle?, *J. Geophys. Res.*, *106*, 13,527–13,540, doi:10.1029/2000JB900378.
- Boschi, L., and T. W. Becker (2011), Vertical coherence in mantle heterogeneity from global seismic data, *Geophys. Res. Lett.*, *38*, L20306, doi:10.1029/2011GL049281.
- Boschi, L., and A. M. Dziewoński (2000), Whole Earth tomography from delay times of P, PcP, PKP phases: Lateral heterogeneities in the outer core or radial anisotropy in the mantle?, *J. Geophys. Res.*, *105*, 25,567–25,594, doi:10.1029/2000JB900059.
- Boschi, L., and G. Ekström (2002), New images of the Earth's upper mantle from measurements of surface-wave phase velocity anomalies, *J. Geophys. Res.*, *107*(B4), 2059, doi:10.1029/2000JB000059.
- Boschi, L., G. Ekström, and B. Kustowski (2004), Multiple resolution surface wave tomography: The Mediterranean Basin, *Geophys. J. Int.*, *157*, 293–304, doi:10.1111/j.1365-246X.2004.02194.x.
- Boschi, L., T. W. Becker, and B. Steinberger (2008), On the statistical significance of correlations between synthetic mantle plumes and tomographic models, *Phys. Earth Planet. Inter.*, *167*, 230–238, doi:10.1016/j.pepi.2008.03.009.
- Boschi, L., B. Fry, G. Ekström, and D. Giardini (2009), The European upper mantle as seen by surface waves, *Surv. Geophys.*, *30*, 463–501, doi:10.1007/s10712-009-9066-2.
- Bozdag, E., and J. Trampert (2008), On crustal corrections in surface wave tomography, *Geophys. J. Int.*, *172*(3), 1066–1082, doi:10.1111/j.1365-246X.2007.03690.x.
- Bull, A. L., A. McNamara, T. W. Becker, and J. Ritsema (2010), Global scale models of the mantle flow field predicted by synthetic tomography models, *Phys. Earth Planet. Inter.*, *182*, 129–138, doi:10.1016/j.pepi.2010.03.004.
- Dahlen, F. A., and J. Tromp (1998), *Theoretical Global Seismology*, Princeton Univ. Press, Princeton, N. J.
- Debayle, E., and Y. Ricard (2012), A global shear velocity model of the upper mantle from fundamental and higher Rayleigh mode measurements, *J. Geophys. Res.*, *117*, B10308, doi:10.1029/2012JB009288.
- Della Mora, S., L. Boschi, P. J. Tackley, T. Nakagawa, and D. Giardini (2011), Low seismic resolution cannot explain S/P decorrelation in the lower mantle, *Geophys. Res. Lett.*, *38*, L12303, doi:10.1029/2011GL047559.
- Dziewoński, A., and B. Romanowicz (2007), Seismology and structure of the Earth, in *Treatise on Geophysics*, pp. 1–29, Elsevier, Amsterdam, Netherlands.
- Dziewoński, A. M., and D. L. Anderson (1981), Preliminary reference Earth model, *Phys. Earth Planet. Inter.*, *25*, 297–356, doi:10.1016/0031-9201(81)90046-7.
- Ekström, G. (2011), A global model of Love and Rayleigh surface wave dispersion and anisotropy, 25–250 s, *Geophys. J. Int.*, *187*(3), 1668–1686, doi:10.1111/j.1365-246X.2011.05225.x.
- Ekström, G., and A. M. Dziewoński (1998), The unique anisotropy of the Pacific upper mantle, *Nature*, *394*, 168–172, doi:10.1038/28148.
- Ferreira, A. M., J. H. Woodhouse, K. Visser, and J. Trampert (2010), On the robustness of global radially anisotropic surface wave tomography, *J. Geophys. Res.*, *115*, B04313, doi:10.1029/2009JB006716.
- Forsyth, D. W. (1975), The early structural evolution and anisotropy of the oceanic upper mantle, *Geophys. J. R. Astron. Soc.*, *43*, 103–162, doi:10.1111/j.1365-246X.1975.tb00630.x.
- Fouch, M. J., and S. Rondenay (2006), Seismic anisotropy beneath stable continental interiors, *Phys. Earth Planet. Inter.*, *158*, 292–320, doi:10.1016/j.pepi.2006.03.024.
- French, S., V. Lekić, and B. Romanowicz (2013), Waveform tomography reveals channeled flow at the base of the oceanic asthenosphere, *Science*, *342*, 227–230, doi:10.1126/science.1241514.
- Grand, S. P., R. D. van der Hilst, and S. Widiyantoro (1997), Global seismic tomography: A snapshot of convection in the Earth, *GSA Today*, *7*, 1–7.
- Gu, Y. H., A. L. Lerner-Lam, A. M. Dziewoński, and G. Ekström (2005), Deep structure and seismic anisotropy beneath the East Pacific Rise, *Earth Planet. Sci. Lett.*, *232*, 259–272, doi:10.1016/j.epsl.2005.01.019.
- Gung, Y., M. Panning, and B. Romanowicz (2003), Global anisotropy and the thickness of continents, *Nature*, *422*, 707–711, doi:10.1038/nature01559.

- Hansen, P. C. (1992), Analysis of discrete ill-posed problems by means of the L-curve, *SIAM Rev.*, *34*(4), 561–580.
- Hess, H. H. (1964), Seismic anisotropy of the uppermost mantle under oceans, *Nature*, *203*, 629–631, doi:10.1038/203629a0.
- Jordan, T. H. (1981), Global tectonic regionalization for seismological data Analysis, *Bull. Seismol. Soc. Am.*, *71*, 1131–1141.
- Kawai, K., and R. J. Geller (2010), Waveform inversion for localized seismic structure and an application to D" structure beneath the Pacific, *J. Geophys. Res.*, *115*, B01305, doi:10.1029/2009JB006503.
- Kawakatsu, H., and S. Yoshioka (2011), Metastable olivine wedge and deep dry cold slab beneath southwest Japan, *Earth Planet. Sci. Lett.*, *303*, 1–10, doi:10.1016/j.epsl.2011.01.008.
- Kawakatsu, H., P. Kumar, Y. Takei, M. Shinohara, T. Kanazawa, E. Araki, and K. Suyehiro (2009), Seismic evidence for sharp lithosphere-asthenosphere boundaries of oceanic plates, *Science*, *324*, 499–502, doi:10.1126/science.1169499.
- Kumar, P., and H. Kawakatsu (2011), Imaging the seismic lithosphere-asthenosphere boundary of the oceanic plate, *Geochem. Geophys. Geosyst.*, *12*, Q01006, doi:10.1029/2010GC003358.
- Kustowski, B., A. M. Dziewonski, and G. Ekström (2007), Nonlinear crustal corrections for normal-mode seismograms, *Bull. Seismol. Soc. Am.*, *97*, 1756–1762, doi:10.1785/0120070041.
- Kustowski, B., G. Ekström, and A. M. Dziewoński (2008), Anisotropic shear-wave velocity structure of the Earth's mantle: A global model, *J. Geophys. Res.*, *113*, B06306, doi:10.1029/2007JB005169.
- Laske, G., G. Masters, Z. Ma, and M. Pasyanos (2013), Update on CRUST1.0—A 1-degree Global Model of Earth's Crust, *Geophys. Res. Abstr.*, *15*, EGU2013-2658.
- Lebedev, S., and R. D. van der Hilst (2008), Global upper-mantle tomography with the automated multimode inversion of surface and S-wave forms, *Geophys. J. Int.*, *173*, 505–518, doi:10.1111/j.1365-246X.2008.03721.x.
- Lekić, V., and B. Romanowicz (2011), Inferring upper-mantle structure by full waveform tomography with the spectral element method, *Geophys. J. Int.*, *185*, 799–831, doi:10.1111/j.1365-246X.2011.04969.x.
- Lekić, V., M. Panning, and B. Romanowicz (2010), A simple method for improving crustal corrections in waveform tomography, *Geophys. J. Int.*, *182*(1), 265–278, doi:10.1111/j.1365-246X.2010.04602.x.
- Li, C., R. D. van der Hilst, E. R. Engdahl, and S. Burdick (2008), A new global model for P wave speed variations in Earth's mantle, *Geochem. Geophys. Geosyst.*, *9*, Q05018, doi:10.1029/2007GC001806.
- Li, X.-D., and B. Romanowicz (1996), Global mantle shear velocity model developed using nonlinear asymptotic coupling theory, *J. Geophys. Res.*, *101*(B10), 22,245–22,272, doi:10.1029/96JB01306.
- Long, M. D., and T. W. Becker (2010), Mantle dynamics and seismic anisotropy, *Earth Planet. Sci. Lett.*, *297*, 341–354.
- Love, A. E. H. (1927), *A Treatise on the Mathematical Theory of Elasticity*, Cambridge Univ. Press, Cambridge, reprinted in 1944 by Dover Publications, New York.
- Mégnin, C., H.-P. Bunge, B. Romanowicz, and M. A. Richards (1997), Imaging 3-D spherical convection models: What can seismic tomography tell us about mantle dynamics?, *Geophys. Res. Lett.*, *24*, 1299–1302, doi:10.1029/97GL01256.
- Menke, W. (1989), *Geophysical Data Analysis: Discrete Inverse Theory. Revised Edition*, Acad. Press, San Diego, Calif.
- Montagner, J.-P. (1998), Where can seismic anisotropy be detected in the Earth's mantle? In boundary layers, *Pure Appl. Geophys.*, *151*, 223–256.
- Montagner, J.-P., and D. L. Anderson (1989), Petrological constraints on seismic anisotropy, *Phys. Earth Planet. Inter.*, *54*, 82–105, doi:10.1016/0031-9201(89)90189-1.
- Montagner, J.-P., and H.-C. Nataf (1986), A simple method for inverting the azimuthal anisotropy of surface waves, *J. Geophys. Res.*, *91*, 511–520, doi:10.1029/JB091iB01p00511.
- Nettles, M., and A. M. Dziewoński (2008), Radially anisotropic shear-velocity structure of the upper mantle globally and beneath North America, *J. Geophys. Res.*, *113*, B02303, doi:10.1029/2006JB004819.
- Nolet, G. (1990), Partitioned waveform inversion and two-dimensional structure under the network of autonomously recording seismographs, *J. Geophys. Res.*, *95*(B6), 8499–8512, doi:10.1029/JB095iB06p08499.
- Nolet, G. (2008), *A Breviary of Seismic Tomography*, Princeton Univ. Press, Cambridge Univ. Press, Cambridge, U. K.
- Paige, C. C., and M. A. Saunders (1982), LSQR: An algorithm for sparse linear equations and sparse least square problems, *Trans. Math. Software*, *8*, 43–71, doi:10.1145/355984.355989.
- Panning, M., and B. Romanowicz (2006), A three-dimensional radially anisotropic model of shear velocity in the whole mantle, *Geophys. J. Int.*, *167*, 361–379, doi:10.1111/j.1365-246X.2006.03100.x.
- Panning, M. P., V. Lekić, and B. A. Romanowicz (2010), Importance of crustal corrections in the development of a new global model of radial anisotropy, *J. Geophys. Res.*, *115*, B12325, doi:10.1029/2010JB007520.
- Podolefsky, N. S., S. Zhong, and A. K. McNamara (2004), The anisotropic and rheological structure of the oceanic upper mantle from a simple model of plate shear, *Geophys. J. Int.*, *158*, 287–296, doi:10.1111/j.1365-246X.2004.02250.x.
- Qin, Y., Y. Capdeville, J.-P. Montagner, L. Boschi, and T. W. Becker (2009), Reliability of mantle tomography models assessed by spectral-element simulations, *Geophys. J. Int.*, *177*, 125–144.
- Raitt, R. W., G. G. Shor Jr., G. B. Morris, and H. K. Kirk (1971), Mantle anisotropy in the Pacific Ocean, *Tectonophysics*, *12*(3), 173–186, doi:10.1016/0040-1951(71)90002-3.
- Revenaugh, J., and T. H. Jordan (1991), Mantle layering from ScS reverberations: 3. The upper mantle, *J. Geophys. Res.*, *96*, 19,781–19,810, doi:10.1029/91JB01487.
- Ritsema, J., and H. J. van Heijst (2000), Seismic imaging of structural heterogeneity in Earth's mantle: Evidence for large-scale mantle flow, *Sci. Prog.*, *83*, 243–259.
- Ritsema, J., H. J. van Heijst, and J. H. Woodhouse (2004), Global transition zone tomography, *J. Geophys. Res.*, *109*, B02302, doi:10.1029/2003JB002610.
- Ritsema, J., A. K. McNamara, and A. L. Bull (2007), Tomographic filtering of geodynamic models: Implications for model interpretation and large-scale mantle structure, *J. Geophys. Res.*, *112*, B01303, doi:10.1029/2006JB004566.
- Ritsema, J., H. J. van Heijst, A. Deuss, and J. H. Woodhouse (2011), S40RTS: A degree-40 shear velocity model for the mantle from new Rayleigh wave dispersion, teleseismic traveltimes, and normal-mode splitting function measurements, *Geophys. J. Int.*, *184*, 1223–1236.
- Sambridge, M., and K. Mosegaard (2002), Monte Carlo methods in geophysical inverse problems, *Rev. Geophys.*, *40*(3), 1009, doi:10.1029/2000RG000089.
- Schaefer, J. F., L. Boschi, and E. Kissling (2011), Adaptively parametrized surface wave tomography: Methodology and a new model of the European upper mantle, *Geophys. J. Int.*, *186*(3), 1431–1453, doi:10.1111/j.1365-246X.2011.05135.x.
- Schaefer, A. J., and S. Lebedev (2013), Global shear speed structure of the upper mantle and transition zone, *Geophys. J. Int.*, *194*(2), 417–449, doi:10.1093/gji/ggt095.

- Schmerr, N. (2012), The Gutenberg discontinuity: Melt at the lithosphere-asthenosphere boundary, *Science*, 335(6075), 1480–1483, doi:10.1126/science.1215433.
- Siglloch, K. (2011), Mantle provinces under North America from multifrequency P wave tomography, *Geochem. Geophys. Geosyst.*, 12, Q02W08, doi:10.1029/2010GC003421.
- Silver, P. G. (1996), Seismic anisotropy beneath the continents: Probing the depths of geology, *Annu. Rev. Earth Planet. Sci.*, 24, 385–432, doi:10.1146/annurev.earth.24.1.385.
- Simmons, N. A., A. M. Forte, L. Boschi, and S. P. Grand (2010), GyPSuM: A joint tomographic model of mantle density and seismic wave speeds, *J. Geophys. Res.*, 115, B12310, doi:10.1029/2010JB007631.
- Simons, F. J., I. Loris, G. Nolet, I. C. Daubechies, S. Voronin, J. S. Judd, P. A. Vettera, J. Charley, and C. Vonesch (2011), Solving or resolving global tomographic models with spherical wavelets, and the scale and sparsity of seismic heterogeneity, *Geochem. Geophys. Geosyst.*, 12(2), 969–988, doi:10.1111/j.1365-246X.2011.05190.
- Smith, M. L., and F. A. Dahlen (1973), The azimuthal dependence of Love and Rayleigh wave propagation in a slightly anisotropic medium, *J. Geophys. Res.*, 78, 3321–3333, doi:10.1029/JB078i017p03321.
- Soldati, G., L. Boschi, and A. Piersanti (2003), Outer core density heterogeneity and the discrepancy between PKP and PcP travel time observations, *Geophys. Res. Lett.*, 30(4), 1190, doi:10.1029/2002GL016647.
- Tan, Y., and D. V. Helmberger (2007), Trans-Pacific upper mantle shear velocity structure, *J. Geophys. Res.*, 112, B08301, doi:10.1029/2006JB004853.
- van Heijst, H. J., and J. Woodhouse (1997), Measuring surface-wave overtone phase velocities using a mode-branch stripping technique, *Geophys. J. Int.*, 131(2), 209–230, doi:10.1111/j.1365-246X.1997.tb01217.x.
- Vinnik, L., G. L. Kosarev, and L. I. Makeyeva (1984), Anisotropy of the lithosphere from the observations of SKS and SKKS phases, *Proc. Acad. Sci. USSR*, 278, 1335–1339.
- Visser, K., J. Trampert, and B. L. N. Kennett (2008a), Global anisotropic phase velocity maps for higher mode Love and Rayleigh waves, *Geophys. J. Int.*, 172(3), 1016–1032, doi:10.1111/j.1365-246X.2007.03685.x.
- Visser, K., J. Trampert, S. Lebedev, and B. L. N. Kennett (2008b), Probability of radial anisotropy in the deep mantle, *Earth Planet. Sci. Lett.*, 270, 241–250.
- Walker, A. M., A. M. Forte, J. Wookey, A. Nowacki, and J.-M. Kendall (2011), Elastic anisotropy of D'' predicted from global models of mantle flow, *Geochem. Geophys. Geosyst.*, 12, Q10006, doi:10.1029/2011GC003732.
- Woodhouse, J. (1981), A note on the calculation of travel times in a transversely isotropic Earth model, *Phys. Earth Planet. Inter.*, 25(4), 357–359.
- Wortel, M. J. R., and W. Spakman (2000), Subduction and slab detachment in the Mediterranean-Carpathian region, *Science*, 209, 1910–1917, doi:10.1126/science.290.5498.1910.